

# Turbulent/turbulent interfacial layers of a shearless turbulence mixing layer in temporally evolving grid turbulence

Cite as: Phys. Fluids **35**, 045117 (2023); <https://doi.org/10.1063/5.0141253>

Submitted: 04 January 2023 • Accepted: 14 March 2023 • Published Online: 04 April 2023

Kohtaro Nakamura (中村 浩太郎),  Tomoaki Watanabe (渡邊 智昭) and  Koji Nagata (長田 孝二)



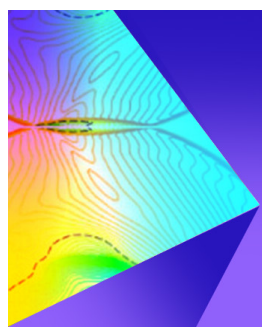
View Online



Export Citation



CrossMark



**Physics of Fluids**  
Special Topic: Shock Waves  
**Submit Today!**

# Turbulent/turbulent interfacial layers of a shearless turbulence mixing layer in temporally evolving grid turbulence

Cite as: Phys. Fluids **35**, 045117 (2023); doi: 10.1063/5.0141253

Submitted: 4 January 2023 · Accepted: 14 March 2023 ·

Published Online: 4 April 2023



View Online



Export Citation



CrossMark

Kohtaro Nakamura (中村 浩太郎),<sup>1</sup> Tomoaki Watanabe (渡邊 智昭),<sup>2,a)</sup>  and Koji Nagata (長田 孝二)<sup>1,b)</sup> 

## AFFILIATIONS

<sup>1</sup>Department of Aerospace Engineering, Nagoya University, Furo-cho, Chikusa, Nagoya 464-8603, Japan

<sup>2</sup>Education and Research Center for Flight Engineering, Nagoya University, Furo-cho, Chikusa, Nagoya 464-8603, Japan

<sup>a)</sup>Author to whom correspondence should be addressed: [watanabe.tomoaki@c.nagoya-u.jp](mailto:watanabe.tomoaki@c.nagoya-u.jp)

<sup>b)</sup>Current address: Department of Mechanical Engineering and Science, Kyoto University, Kyoto 615-8530, Japan.

## ABSTRACT

Turbulent/turbulent interfacial (TTI) layers are investigated with direct numerical simulation of temporally evolving grid turbulence. The present study considers a temporally evolving wake of two parallel-bar grids with different mesh sizes, which generate homogeneous isotropic turbulent regions with large and small turbulent kinetic energies (TKE). A shearless mixing layer of turbulence forms between the large- and small-TKE regions. The TTI layer bounded by the large- or small-TKE region is identified with a passive scalar field, and the flow statistics are evaluated as functions of a position with respect to the TTI layer. Statistics of a velocity gradient tensor suggest that the center and edges of the TTI layer are dominated by vortex sheets and vortex tubes, respectively. Because of the configuration of these vortical structures, the flow toward the TTI layer in the layer-normal direction generates a compressive strain, which is important to sustain the thin layer structure. The mean velocity jump due to the compressive strain is about  $3u_\eta$  and is observed over a length of about  $20\eta$ , where  $u_\eta$  and  $\eta$  are the Kolmogorov velocity and length scales, respectively. The thickness of the TTI layer is about  $12\eta$ , which hardly depends on time. The TTI layer has a large surface area when it is bounded by the large-TKE region. Consequently, the shearless mixing layer tends to entrain more amount of fluid from the large-TKE region than from the small-TKE region although the entrainment rate per unit surface area normalized by the Kolmogorov velocity is similar for both regions.

Published under an exclusive license by AIP Publishing. <https://doi.org/10.1063/5.0141253>

## I. INTRODUCTION

Turbulence plays an important role in flows observed in engineering applications and the environment.<sup>1</sup> It contributes to a high rate of mixing of momentum, kinetic energy, heat, and chemical substances.<sup>2</sup> Flow instabilities often generate a localized turbulent spot, which is separated from outer irrotational (non-turbulent) flow regions. For example, ocean mixing layers become locally turbulent by Kelvin–Helmholtz instability.<sup>3</sup> When a turbulent region is bounded by a non-turbulent region, these regions are separated by a thin layer called a turbulent/non-turbulent interfacial (TNTI) layer.<sup>4</sup> The TNTI layer is important in the entrainment process, by which the turbulent flow entrains the non-turbulent fluid across the TNTI layer.<sup>5–7</sup> This process is also important in understanding turbulent mixing because turbulent and non-turbulent flow regions usually have different flow properties.<sup>8–12</sup> The turbulent and non-turbulent regions can be distinguished by vorticity. Therefore, the properties of the TNTI layer have been extensively studied by detecting the TNTI layer with vorticity

profiles in various turbulent flows, such as jets,<sup>13</sup> wakes,<sup>14,15</sup> mixing layers,<sup>16</sup> boundary layers,<sup>17,18</sup> and a flow around an airfoil.<sup>19</sup>

The TNTI layer is observed when turbulence is bounded by an irrotational flow. A more general case is a problem where two turbulent flows with different length, velocity, and time scales of fluid motions interact with each other. In this case, an interfacial layer, called a turbulent/turbulent interfacial (TTI) layer, forms between two turbulent regions.<sup>4</sup> Because different sources of turbulence often exist in a flow, the TTI layer can be more frequently observed than the TNTI layer in engineering applications. In laboratory experiments, the TTI layer is observed when turbulence is generated in a turbulent environment. For example, wind tunnel experiments are often conducted for a turbulent boundary layer in freestream turbulence.<sup>20</sup> Similarly, a turbulent wake generated by an object placed in freestream turbulence was also studied in a water flume and wind tunnel.<sup>21–24</sup> In addition, a turbulent jet issued into homogeneous isotropic turbulence was investigated in a water tank.<sup>12,25</sup> These studies often distinguish a turbulent

shear flow from external turbulence with a passive scalar, such as a dye concentration, and have confirmed that two turbulent regions are separated by a thin interfacial layer. The conditional average originally developed for the TNTI layer<sup>14</sup> has also been adapted in the studies of the TTI layer, whose properties are examined with conditional statistics calculated as functions of a position with respect to the TTI layer.

Mean-shear effects are important for the behavior of the TNTI layer.<sup>4</sup> Some models of the TNTI layer assume that the shear due to a mean flow is concentrated within the TNTI layer.<sup>26</sup> Therefore, a comparison of the TNTI layers in turbulence with and without mean shear is one of the important subjects in previous studies. Wolf *et al.* have compared the local entrainment rate between a turbulent jet and shear-free turbulence and observed that the local entrainment is enhanced by the mean shear.<sup>27</sup> An inhomogeneous mean flow also leads to the dependence of the TNTI layer on the interface orientation with respect to the mean-flow direction.<sup>28</sup> This mean-shear effects associated with the interface orientation have proved to be important in turbulent mixing near the TNTI layer.<sup>29</sup> To isolate the properties of the TNTI layer from the mean-shear effects, the TNTI layer is often investigated in shear-free turbulence.<sup>30</sup> However, the TTI layer in shear-free turbulence has hardly been studied in the existing literature.

The TNTI layer in shear-free turbulence can be observed in wind tunnel experiments with a turbulence-generating grid that covers a part of the cross-section of the wind tunnel.<sup>31</sup> Screens are also introduced for the remaining part of the cross-section to produce a uniform mean flow in the wind tunnel, where the TNTI layer forms at the edge of grid turbulence without mean shear. Similarly, the TTI layer in shear-free turbulence can be generated with a grid with two length scales.<sup>32–35</sup> The grid often consists of two turbulence-generating grids with different mesh sizes and the same blockage ratio, which are designed to generate turbulence with two different scales in a uniform mean flow. A shearless turbulence mixing layer appears between two quasi homogeneous isotropic regions of turbulence generated by the grid and the TTI layer forms at the edges of the shearless mixing layer.<sup>31,36</sup> This flow setup is particularly useful to investigate the TTI layer without mean shear in experiments. Although wind tunnel experiments have been conducted for the shearless mixing layer of grid turbulence, investigations of the TTI layers are difficult because of the complicated three-dimensional geometry of the interface.

The relation between the TNTI layer and the entrainment in turbulent free shear flows is one of the most important topics because the flow spatially develops by entraining non-turbulent fluid into the turbulent region. Some physical models for the entrainment assume that small-scale vortical structures near the TNTI layer locally entrain the non-turbulent fluids. This entrainment process is called “nibbling” while the entrainment caused by large-scale vortices is often called “engulfment.”<sup>4</sup> The statistics taken near the TNTI layer suggested that the entrainment is dominated by the nibbling process due to small-scale turbulent motions<sup>5,7,13,37,38</sup> although how small-scale vortices cause the entrainment was not fully understood from the flow statistics within the TNTI layer. Then, the characteristics of small-scale vortices within the TNTI layer have been studied with vortex identification schemes.<sup>16,28,39,40</sup> A comparison between vortical structures within the TNTI layer and an ideal vortex, such as Burgers’ vortex, has revealed a physical mechanism of nibbling by vortex tubes, which is explained by a two-stage process: velocity induced by the strain acting on the vortex initially transfers the non-turbulent fluid toward the TNTI layer, and

then, the inertial rotating motion of the vortex transfers the entrained fluid to the turbulent core region.<sup>41</sup> This explanation based on the vortex is consistent with Lagrangian statistics of entrained fluid particles, for which the root mean square of the relative location between the particles and the outer edge of the TNTI layer,  $\delta$ , increases with time as  $\delta \sim t$  in the first stage while the Richardson-like scaling of the inertial range  $\delta \sim t^{3/2}$  prevails in the second stage.<sup>7</sup>

Previous studies on the TNTI layer suggest that it is of great importance to investigate the entrainment characteristics from a viewpoint of the TTI layer to understand the evolution of turbulent flows in a turbulent environment. As also found for the nibbling mechanism for the TNTI layer, vortical structures within the TTI layers may play a dominant role in the entrainment process. However, most previous studies discussed above focused on the variation of flow statistics across the TTI layer without much attention to vortical structures. In addition, experiments were mostly conducted for turbulent shear flows developing in a turbulent environment. Since the TTI layer is expected to be influenced by mean shear, an investigation of the TTI layer without mean shear may shed light on the essential properties of the TTI layer. For these reasons, the present study aims to reveal the vortical structures and entrainment in the TTI layer in a turbulent flow without mean shear. We have carried out direct numerical simulation (DNS) of a shearless turbulence mixing layer of temporally evolving grid turbulence.<sup>42</sup> Turbulence is generated by parallel-bar grids with two different mesh sizes. The shearless mixing layer develops between two quasi-homogeneous-isotropic regions generated by the grids. The TTI layers form at the edges of the shearless mixing layer, for which the statistics related to the TTI layers are evaluated.

The paper is organized as follows: Sec. II describes the DNS database of temporally evolving grid turbulence. Section III presents the results of the statistical analyses of the TTI layer. The statistics plotted as functions of the position with respect to the TTI layer are used to examine the layer thickness, the layer structures, and the entrainment rate across the layer. Finally, the paper is summarized in Sec. IV.

## II. DNS DATABASE OF A SHEARLESS TURBULENCE MIXING LAYER IN TEMPORALLY EVOLVING GRID TURBULENCE

The present DNS considers a temporally evolving turbulent wake of a grid. A temporal model of turbulent wakes has widely been used in fundamental studies of turbulence.<sup>15,43–45</sup> A spatially evolving wake, which is often studied with wind tunnel experiments, is not homogeneous in the streamwise ( $x$ ) direction. However, in a fully developed wake, flow statistics vary more drastically in the transverse direction than in the  $x$  direction. Because of the very slow variation of statistics in the  $x$  direction, turbulence can be treated approximately as homogeneous in this direction in the temporal model of wakes. Then, the temporal wake develops with time in a computational domain which is periodic in the  $x$  direction. This approximation is not expected to be valid in the near region just behind an object. At least, the wake behavior in the far field is very similar between temporal and spatial wakes.<sup>15,43–45</sup> Similar temporally evolving turbulence has been studied for various turbulent shear flows, such as jets, mixing layers, and boundary layers, for which the temporally evolving flows behave similarly to spatial ones.<sup>16,46–51</sup>

The present study adapts the methodology of temporal wakes to grid turbulence, which is generated by a wake of a grid. Similar to

temporally evolving wakes, the periodic boundary conditions are applied in the  $x$  direction. The temporal wake is simulated without including an object in a computational domain. A mean velocity profile of the initial condition approximates a velocity deficit behind an object.<sup>15</sup> Here, as the temporal wake assumes the statistical homogeneity in the  $x$  direction, the initial mean velocity is also homogeneous in the  $x$  direction and depends only on the transverse positions in the wake. For the same reason, the grid itself is not embedded in the computational domain in simulations of temporally evolving grid turbulence. The temporally evolving grid turbulence is a numerical model that approximates grid turbulence in experiments. However, the evolution of velocity variance is quantitatively consistent between temporal and spatial grid turbulence in the near- and far-fields.<sup>52,53</sup>

Turbulence-generating grids are often used with wind tunnels or water flumes, where the grid is installed in a uniform mean flow.<sup>54–60</sup> Another type of grid turbulence is generated in towed-grid experiments, in which a grid is towed at a constant speed in water in a tank. The wake of the grid generates turbulence with small volume-averaged velocity in the water tank.<sup>21,61–63</sup> Once grid turbulence is generated in the tank, turbulence decays with time. The present DNS corresponds to temporal simulations of these towed-grid experiments. Because grid turbulence in wind tunnels has rms velocity fluctuations much smaller than the mean velocity, instantaneous streamwise velocity is always positive. However, turbulence generated by a towed grid does not have a strong mean flow, and both positive and negative values of streamwise velocity are observed.

### A. DNS of temporally evolving grid turbulence of a parallel-bar grid

The DNS database of temporally evolving grid turbulence<sup>42</sup> is used to investigate the shearless turbulence mixing layer. Fundamental statistics of velocity are discussed for the development of grid turbulence in Ref. 42. DNS has been performed for temporally evolving grid turbulence with a transfer of passive scalar  $\phi$ . The governing equations are the Navier–Stokes equations and scalar transport equation for an incompressible fluid:

$$\frac{\partial u_j}{\partial x_j} = 0, \quad (1)$$

$$\frac{\partial u_i}{\partial t} + \frac{\partial u_i u_j}{\partial x_j} = -\frac{1}{\rho} \frac{\partial p}{\partial x_i} + \nu \frac{\partial^2 u_i}{\partial x_j \partial x_j}, \quad (2)$$

$$\frac{\partial \phi}{\partial t} + \frac{\partial u_j \phi}{\partial x_j} = D \frac{\partial^2 \phi}{\partial x_j \partial x_j}. \quad (3)$$

Here,  $u_i$  is the  $i$ th component of the velocity vector,  $x_i$  is the position in the  $i$  direction,  $t$  is time,  $p$  is the pressure,  $\rho$  is a constant density of the fluid,  $\nu$  is the kinematic viscosity, and  $D$  is the diffusivity coefficient for  $\phi$ . The streamwise, spanwise, and vertical directions are denoted by  $x$ ,  $y$ , and  $z$ , respectively, while the velocity components in these directions are  $u$ ,  $v$ , and  $w$ .

A turbulence-generating grid used in wind tunnel experiments in Ref. 35 is considered in the DNS. The grid consists of two parallel-bar grids shown in Fig. 1. Grids 1 and 2 have mesh sizes of  $M_1$  and  $M_2$  with  $M_2 = 0.284M_1$ . The thicknesses of the bars consisting of grids 1 and 2 are denoted by  $d_1$  and  $d_2$ , respectively. The solidity of both grids is  $\sigma = 0.35$ , which determines the thicknesses,  $d_1/M_1$  and  $d_2/M_2$ , as

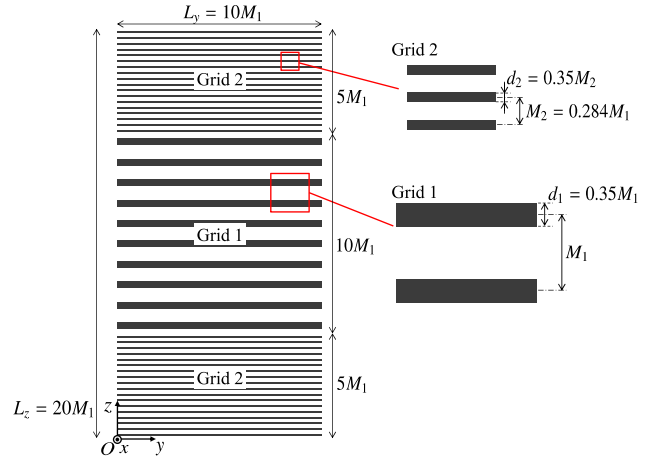


FIG. 1. A parallel-bar grid with two mesh sizes.

shown in Fig. 1. The height of grid 1 in the  $z$  direction is  $10M_1$ . Grid 2 is located above and below grid 1, and each region of grid 2 has a height of  $5M_1$ .

The numerical methods are briefly described here while the details have been presented in Ref. 42. The DNS uses a rectangular computational domain with a size of  $(L_x, L_y, L_z) = (10M_1, 10M_1, 20M_1)$ . Here,  $L_z$  is large enough for turbulence generated by each grid to be homogeneous and isotropic, as confirmed in Ref. 42. The flow is initialized with a mean velocity profile which approximates the velocity deficit of the wake. The periodic boundary conditions are applied in three directions. The flow is statistically homogeneous in the  $x$  and  $y$  directions, and the statistics can be defined with an  $x$ - $y$  average taken as a function of  $z$  and  $t$ . For example, an average of  $f(x, y, z, t)$  is calculated as  $\langle f \rangle(z, t) = (1/L_x L_y) \int \int f dx dy$ . The fluctuations from the average are  $f'(x, y, z, t) = f - \langle f \rangle$ . The initial velocity profile consists of a mean velocity vector  $(\langle u \rangle, 0, 0)$  and fluctuating components  $(u', v', w')$ . Different values are assigned for  $\langle u \rangle$  depending on  $z$ :  $\langle u \rangle/U_0 = 1 - \sigma$  behind the bars of the grids and  $\langle u \rangle/U_0 = -\sigma$  elsewhere. The velocity difference  $U_0$  between the bars and the other regions corresponds to the mean velocity in wind tunnel experiments.<sup>52</sup> Here,  $\sigma$  is subtracted for the volume-averaged velocity to be zero. This enables the DNS to adapt a large time increment  $\Delta t$  at a late time as the order of instantaneous velocity is the same as that of velocity fluctuations when the volume-averaged velocity is zero. In addition, spatially correlated velocity fluctuations  $(u', v', w')$  generated by a diffusive process are superimposed onto the initial mean velocity.<sup>64</sup> The root mean square (rms) of the velocity fluctuations is  $0.5\%$  of  $U_0$ , which is as small as the freestream disturbance in wind tunnel experiments.<sup>55,65</sup> The initial profile of the passive scalar is given by

$$\phi = \frac{\phi_0}{2} + \frac{\phi_0}{2} \tanh\left(\frac{10M_1 - 2|z - 10M_1|}{4\theta}\right), \quad (4)$$

for which  $\phi = \phi_0$  and  $0$  in the regions of grids 1 and 2, respectively, and  $\phi$  smoothly varies over a width of  $\theta = 0.05M_1$  between the two regions. As explained below,  $\phi$  is used as a marker of turbulence generated by grid 1. The Reynolds number  $Re = U_0 M_1 / \nu$  is 5000 while the Prandtl number  $Pr = \nu / D$  is 1. A reference timescale of grid 1 is



defined as  $T_r = M_1/U_0$ , which is used to non-dimensionalize time. From the initial conditions described above, the turbulent wakes of the bars are generated because of the mean velocity gradient. Eventually, the mean velocity profile becomes uniform even in the  $z$  direction by the interaction of the wakes. At this stage, quasi homogeneous isotropic turbulence with different levels of turbulent kinetic energy (TKE) forms in the regions of grids 1 and 2, between which the shearless turbulence mixing layer develops.

The DNS was carried out with an in-house DNS code for incompressible turbulent flows, which is based on the fractional step method. The same DNS code has been used in previous studies, where the code has been validated by comparing the results with other numerical simulations and experiments.<sup>53,66</sup> The spatial discretization is based on a fourth-order fully conservative finite difference<sup>67</sup> while the temporal integral is computed with a third-order and low-storage Runge–Kutta method.<sup>68</sup> The Poisson equation for pressure is solved with the biconjugate gradient stabilized method. Temporally evolving grid turbulence simulated with this DNS code was studied in Refs. 52 and 53. In these papers, comparisons were reported for the DNS results with experiments of grid turbulence and theories of isotropic turbulence, confirming that the production and decay regimes of grid turbulence are well reproduced in the DNS. The number of the grid points is  $(N_x, N_y, N_z) = (1024, 1024, 2048)$ . The grid spacing  $\Delta$  is uniform in all directions. The TTI layer is analyzed in the fully developed shearless mixing layer for  $t/T_r \gtrsim 9$ . For the Kolmogorov scale  $\eta = (\nu^3/\langle\epsilon\rangle)^{1/4}$  defined with the kinetic energy dissipation rate  $\epsilon = 2\nu S_{ij}S_{ij}$  and the rate-of-strain tensor  $S_{ij}$ , the resolution  $\Delta$  is about  $1.2\eta$  at  $t/T_r \approx 9$  in the shearless mixing layer. As turbulence decays,  $\eta$  becomes large, ensuring that the resolution is better than  $\Delta = 1.2\eta$ . For the present finite difference schemes,  $\Delta/\eta \lesssim 2$  is sufficient to resolve the energy and dissipation spectra at small scales.<sup>69</sup> DNS of turbulent boundary layers with different resolutions suggest that  $\Delta/\eta \lesssim 1.5$  is required to resolve the geometry of the TNTI layer.<sup>70</sup> The present DNS satisfies these requirements for DNS studies of the interface.

For numerical simulations of spatially evolving grid turbulence, the computational domain should be very long in the  $x$  direction to

observe the decay of turbulence.<sup>71–76</sup> However, temporal grid turbulence decays with time, and the length of the domain in the  $x$  direction can be as small as in the transverse directions. The size in the transverse directions should be much larger than the integral scale to prevent the periodic boundaries from causing unphysical effects on the flow evolution. When the domain size is greater than about 3.3 times the integral scale, the periodic boundaries do not have unphysical effects on decaying turbulence.<sup>77</sup> The integral scale increases with time as turbulence decays. For the integral scale defined with the longitudinal auto-correlation function of streamwise velocity, the domain size  $L_x$  is 18.1 and 21.1 times larger than the integral scales for grids 1 and 2, respectively, when the integral scales reach the maximum at the end of the simulation. Therefore, the domain size is large enough to investigate the decaying turbulence.

### III. RESULTS AND DISCUSSION

#### A. Development of the shearless turbulence mixing layer

The development of the shearless turbulence mixing layer is briefly discussed before the main results for the TTI layer are presented. Figure 2 visualizes the development of grid turbulence with streamwise velocity  $u$  and passive scalar  $\phi$ . At an early time in Fig. 2(a),  $u$  exhibits a pattern of the grid geometry for grid 1. The mean velocity gradient in the initial field results in the development of turbulent wakes. Then, quasi homogeneous isotropic turbulence forms near the center of grids 1 and 2. The timescales of grid turbulence are given by  $M_1/U_0$  and  $M_2/U_0$  for grids 1 and 2, respectively. Because of  $M_1 > M_2$ , turbulence for grid 2 develops faster than that of grid 1. The initial values of  $\phi$  are  $\phi_0$  and 0 for grids 1 and 2, respectively. As confirmed in previous studies of the TTI layer,  $\phi$  can be used as a marker of turbulence generated by grids 1 and 2.<sup>24</sup> Once grid turbulence of these grids has fully developed, the mean velocity gradient becomes negligibly small in the TKE budget.<sup>53</sup> However, the TKE is different for two regions of grid turbulence, between which the TKE smoothly varies in the shearless mixing layer. Grid-turbulence regions generated by grids 1 and 2 can be identified as  $\phi/\phi_0 = 1$  and 0,

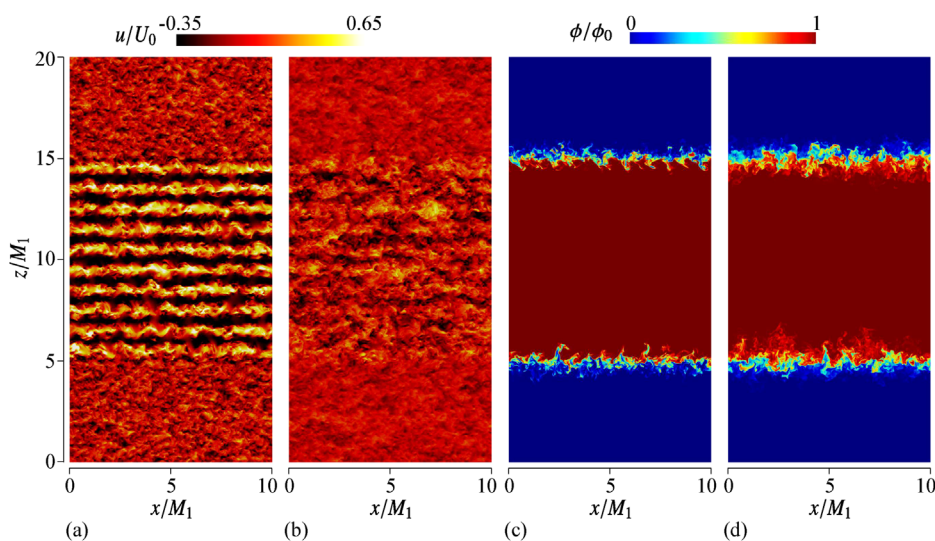


**FIG. 2.** Instantaneous profiles of (a) and (b) streamwise velocity  $u$  and (c) and (d) passive scalar  $\phi$  on an  $x$ - $z$  plane at (a) and (c)  $t/T_r = 4$ , and (b) and (d)  $t/T_r = 7$ .

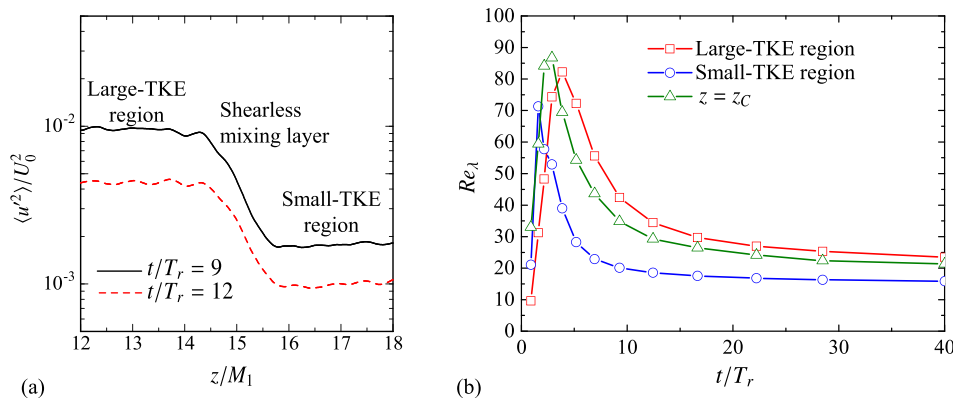


**FIG. 3.** (a) Vertical profiles of the variance of streamwise velocity  $\langle u^2 \rangle$  at  $t/T_r = 9$  and 12. Only a small part of  $z$  in the domain is shown here. (b) Temporal variations of the turbulent Reynolds number  $Re_\lambda$  at the center of the shearless mixing layer and in the large- and small-TKE regions.

respectively, while the shearless mixing layers are identified as  $0 < \phi/\phi_0 < 1$  above and below the turbulent region of grid 1. The temporal development of  $\phi$  suggests that the thickness of the shearless mixing layer increases with time. Similarly, the growth of the layer thickness was also confirmed from the vertical profiles of TKE.<sup>42</sup>

Figure 3(a) plots the variance of streamwise velocity,  $\langle u^2 \rangle$ , as a function of  $z$ . Here, the profile is shown for the shearless mixing layer in the upper region of the grid although the statistically identical shearless mixing layer appears in the lower region. For  $z/M_1 \lesssim 14$  and  $z/M_1 \gtrsim 16$ ,  $\langle u^2 \rangle$  hardly varies with  $z$  because the core regions of grid turbulence are almost homogeneous and isotropic. The turbulence generated by grid 1 ( $z/M_1 \lesssim 14$ ) has a larger TKE than that by grid 2 ( $z/M_1 \gtrsim 16$ ), and they are called large- and small-TKE regions, respectively. The shearless mixing layer, where  $\langle u^2 \rangle$  varies with  $z$ , forms between the large- and small-TKE regions. The center of the shearless mixing layer is identified with the normalized velocity variance:  $\hat{U}(z, t) \equiv (\langle u^2 \rangle - U_S)/(U_L - U_S)$ , where  $U_L$  and  $U_S$  are values of  $\langle u^2 \rangle$  in the large- and small-TKE regions, respectively. For this definition,  $\hat{U}$  varies from 0 to 1 from the small- to large-TKE regions. The center of the shearless mixing layer,  $z_C(t)$ , is defined as the vertical location of  $\hat{U} = 0.5$ . The statistics evaluated at this location are denoted with subscript  $C$  and are used to normalize the statistics of the TTI layer. For example, the Kolmogorov length, velocity, and time scales at  $z = z_C$  are evaluated as  $\eta_C = (\nu^3/\langle \epsilon \rangle_C)^{1/4}$ ,  $u_{\eta C} = (\nu \langle \epsilon \rangle_C)^{1/4}$ , and  $\tau_{\eta C} = (\nu/\langle \epsilon \rangle_C)^{1/2}$ , respectively.

Figure 3(b) shows the temporal evolution of turbulent Reynolds number  $Re_\lambda = \sqrt{\langle u^2 \rangle} \lambda_x / \nu$  at  $z = z_C$  and in the large- and small-TKE regions. Here,  $\lambda_x = \sqrt{\langle u^2 \rangle} / \sqrt{\langle (\partial u' / \partial x)^2 \rangle}$  is the Taylor microscale. In all regions,  $Re_\lambda$  reaches a peak before  $t/T_r = 5$  and then decays with time. In the decay period ( $t/T_r \gtrsim 5$ ),  $Re_\lambda$  becomes small from the large- to small-TKE regions across the shearless mixing layer. Although  $Re_\lambda$  slowly decays with time, other length and velocity scales, such as the Kolmogorov scale and rms velocity fluctuations, vary with time more drastically, as presented in Ref. 42.

Figure 4(a) compares the vertical profiles of normalized deviation of streamwise velocity variance from the value in the small-TKE region,  $\hat{U}$ , between the present DNS and wind tunnel experiments.<sup>32,33</sup> The profiles are shown for the shearless mixing layer in the upper region and for the time for which the TTI layers are analyzed. The vertical coordinate  $z$  is shown as a distance from the center of the shearless mixing layer,  $z - z_C$ . In addition,  $z - z_C$  is normalized by the width of the layer  $\Delta_M$ , which is defined as the distance from  $\hat{U} = 0.25$  to 0.75. Scatters of  $\hat{U}$  become large at a late time because the increase in the integral scale results in fewer statistical samples for large-scale motions, which dominate the velocity variance. Although Veeravalli and Warhaft<sup>32</sup> used a parallel-bar grid, their experiment is different from the DNS in terms of the Reynolds number  $Re = U_0 M_1 / \nu$  and grid parameters,  $M_1/M_2$  and solidity. The decay of grid turbulence is sensitive to the Reynolds number at a low  $Re$  regime considered in the DNS. Thus, a small difference between the DNS and the experiment is

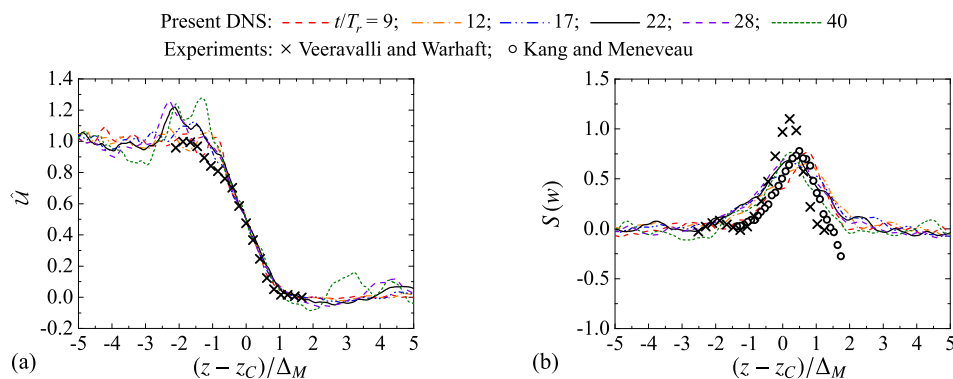


**FIG. 4.** Comparison between the present DNS and wind tunnel experiments of shearless mixing layers by Veeravalli and Warhaft<sup>32</sup> and Kang and Meneveau:<sup>33</sup> vertical profiles of (a) normalized streamwise velocity variance  $\hat{U}$  and (b) skewness of vertical velocity,  $S(w)$ . The results are plotted as a function of the distance from the center of shearless mixing layers,  $z - z_C$ , divided by the layer thickness  $\Delta_M$ . Large- and small-TKE regions are located on the sides of  $z - z_C < 0$  and  $z - z_C > 0$ , respectively.

also anticipated. However, the normalized velocity variance in Fig. 4(a) generally agrees with the experiment.

The shearless mixing layers exhibit an intermittent behavior of large-scale turbulent motions, which is often studied with the skewness of vertical velocity  $S(w) = \langle w^3 \rangle / \langle w^2 \rangle^{3/2}$ , whose vertical profiles are compared between the DNS and experiments in Fig. 4(b). The shearless mixing layer is located for  $|(z - z_C)/\Delta_M| \lesssim 2$ . The experiment by Kang and Meneveau was conducted with a composite grid consisting of an active grid and a static square grid.<sup>33</sup> Despite the differences in the grid geometry and Reynolds number, the variation of  $S(w)$  is consistent with the DNS and experiments:  $S(w) \approx 0$  in the regions of quasi homogeneous isotropic turbulence generated by grids 1 and 2 while  $S(w)$  has a positive peak in the shearless mixing layer. Large-scale vortices in the large-TKE region with  $w \gg 0$  intermittently penetrate the shearless mixing layer, resulting in  $S(w) > 0$ .<sup>32,33</sup> This intermittent behavior is also well reproduced in the present DNS.

Figure 5 shows the one-dimensional longitudinal energy spectrum of streamwise velocity fluctuations at  $z/M_1 = 10$  and 0, which are located at the center of grids 1 and 2, respectively. The streamwise wavenumber  $k_x$  and spectrum  $E_u$  are normalized by the Kolmogorov scale  $\eta$ , energy dissipation rate  $\langle \varepsilon \rangle$ , and kinematic viscosity  $\nu$  for a comparison with other turbulent flows at small scales. The results are presented at an early time, for which  $\eta$  is small compared with a later time. The normalized energy spectrum in a high wavenumber range is known to collapse for different flows. The spectra for both grids 1 and 2 are consistent with other data, confirming that the spatial resolution is sufficient to study small-scale characteristics of the shearless mixing layer.

## B. Statistical analysis of the TTI layer of the shearless turbulence mixing layer

The flow consists of three turbulent regions, which can be identified with the passive scalar, and the TTI layers appear at the edges of the shearless mixing layer. Here, the present analysis is based on previous studies of the TNTI layers in turbulent free shear flows and boundary layers.<sup>14</sup> Comparisons between the interface defined with a passive scalar and enstrophy have been reported for the TNTI layers in various flows.<sup>17,79</sup> The interfaces defined with these quantities are almost identical if the Schmidt number of the scalar is 1. When the Schmidt number is different from 1, the interface location for the

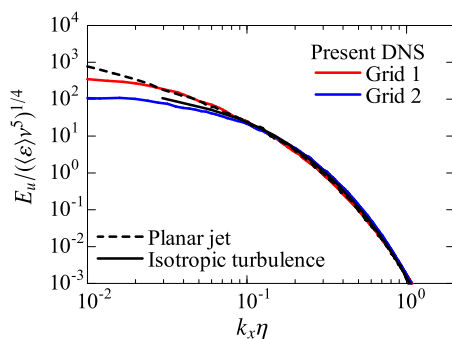


**FIG. 5.** The one-dimensional longitudinal energy spectrum of streamwise velocity fluctuations,  $E_u(k_x)$ , at  $t/T_r = 6$  at the center of grids 1 and 2. The present results are compared with the DNS of a planar jet and isotropic turbulence.<sup>70,78</sup>

passive scalar is slightly different from that for enstrophy<sup>80</sup> although the difference may not be significant enough to affect the statistics calculated near the interface. Similarly, in the case of the TTI layer, the interface defined with a passive scalar successfully detects the region where two turbulent regions with different velocity and length scales are separated.<sup>22</sup> Therefore, the TTI layers between the shearless mixing layer and the large- or small-TKE region are detected with the isosurfaces of  $\phi$ , as indicated by white lines in Fig. 6(a). The isosurfaces of  $\phi/\phi_0 = 0.97$  and 0.03 are used to detect the TTI layers bounded by the large- and small-TKE regions, respectively. Here, these threshold values detect the isosurface within the TTI layers, for which the statistics are evaluated as functions of the position near the isosurfaces. The isosurface locations vary little with a small change of the thresholds because  $\phi$  rapidly changes across the thin TTI layers. Therefore, slightly different choices of the threshold do not alter the conclusion of the paper, as also confirmed in previous studies of the TNTI layers.<sup>4</sup>

The flow characteristics near the TTI layer are examined with conditional statistics calculated as functions of the distance from the isosurface of  $\phi$ . A local interface coordinate  $\zeta_I$  whose origin is placed at the isosurface is introduced for this purpose. For a given point on the isosurface of  $\phi$ , the  $\zeta_I$  direction is taken in the isosurface-normal direction, which is determined by  $\nabla\phi$ . Here,  $\zeta_I$  is defined such that  $\zeta_I < 0$  is in the shearless mixing layer and  $\zeta_I > 0$  is in the large- or small-TKE region. Figure 6(b) illustrates  $\zeta_I$  for the TTI layer bounded by the small-TKE region. The interface coordinate  $\zeta_I$  is defined for many locations on the isosurface. Then, a variable  $f(x, y, z, t)$  defined on the computational grid points is interpolated on  $\zeta_I$  to obtain

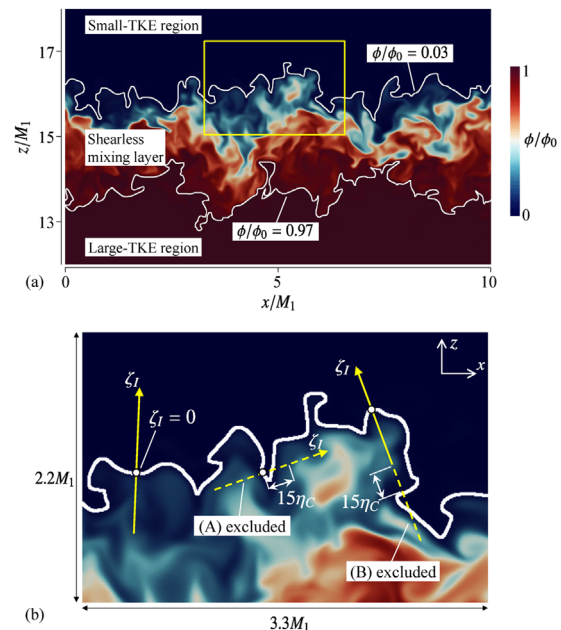


**FIG. 6.** (a) A two-dimensional profile of passive scalar  $\phi$  and interfaces that separate the shearless mixing layer from the large- and small-TKE regions at  $t/T_r = 22$ . White lines are the isosurfaces of  $\phi/\phi_0 = 0.03$  and 0.97. (b) Interface coordinates  $\zeta_I$  for the conditional statistics. The broken lines shown on the coordinates are excluded from the statistical analysis. A region of the yellow box in (a) is shown in (b).

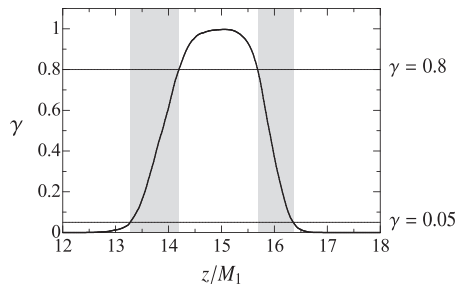


**FIG. 7.** A vertical profile of intermittency factor  $\gamma$  of the shearless mixing layer at  $t/T_r = 17$ . The shaded areas have  $\gamma$  between 0.05 and 0.8 and are used to evaluate the statistics in the intermittent region.

$f(\zeta_I, t)$ . Then, an ensemble average of  $f(\zeta_I, t)$  is taken as a function of  $(\zeta_I, t)$  for all the interface coordinates defined at different locations on the isosurface. This conditional average with  $\zeta_I$  is denoted by  $\langle f \rangle_I$ . Here, the statistics are calculated separately for the isosurfaces of  $\phi/\phi_0 = 0.03$  and  $0.97$  to compare the TTI layers bounded by the small- and large-TKE regions.

The interface coordinate is introduced to calculate the statistics separately for the shearless mixing layer and the other regions. However,  $\zeta_I$  sometimes crosses the isosurface of  $\phi$  even for  $\zeta_I \neq 0$  because of the complicated isosurface geometry. The samples from the shearless mixing layer and the other regions are mixed in this case unless some of the samples are discarded from the analysis. Therefore, a part of  $\zeta_I$  is excluded from the analysis following Refs. 15 and 17. When  $\zeta_I$  crosses the isosurface of  $\phi$  for  $|\zeta_I| < 15\eta_C$ , this interface coordinate is not used to calculate the statistics. This example is shown as A in Fig. 6(b) and is often found for a concave geometry with a small curvature radius. In addition,  $\zeta_I$  within the distance of  $15\eta_C$  from the isosurface at  $\zeta_I \neq 0$  is also excluded from the statistical analysis [B in Fig. 6(b)]. Then, the conditional statistics for  $\zeta_I < 0$  and  $\zeta_I > 0$  are calculated solely from the shearless mixing layer and the large- or small-TKE region, respectively. The distance of  $15\eta_C$  used to discard samples is the same as that used for the conditional statistics of the TNTI layers in previous studies<sup>17</sup> and is determined based on the thickness of the TNTI layer, which is close to the thickness of the TTI layer as shown below.

Figure 7 shows the profile of the intermittency factor  $\gamma$ , which is a probability that the location is within the shearless mixing layer. The center of the shearless mixing layer,  $z/M_1 \approx 15$ , has  $\gamma \approx 1$ , and the fluids of the large- and small TKE regions hardly appear at this location.

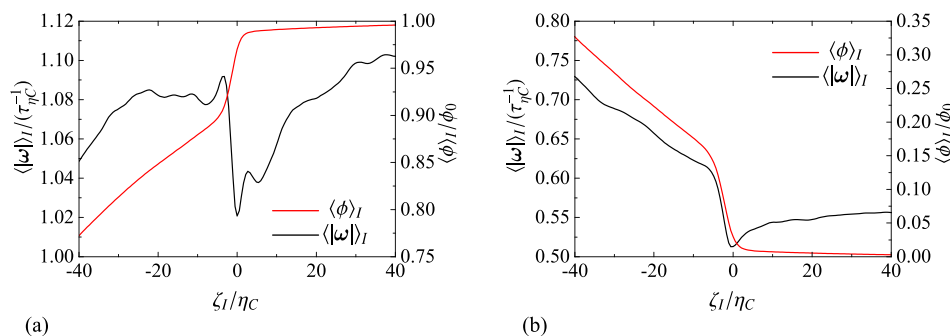


**FIG. 8.** Conditional averages of passive scalar  $\phi$  and vorticity magnitude  $|\omega|$  at  $t/T_r = 22$  near the TTI layers bounded by (a) the large-TKE region and (b) the small-TKE region.

As being away from the center of the shearless mixing layer,  $\gamma$  decreases and eventually becomes 0 in the large- and small-TKE regions. The regions with  $0 < \gamma < 1$  are the intermittent regions, where both the shearless mixing layer and the large- and small-TKE regions are observed. The statistical properties of the shearless mixing layer in the intermittent region are evaluated with an average taken over  $z$  with  $0.05 \leq \gamma \leq 0.8$ . The sample for this average is taken only from the points within the shearless mixing layer ( $0.03 \leq \phi/\phi_0 \leq 0.97$ ) and is also calculated separately for each side of the large- or small-TKE region. The statistics calculated with  $\gamma$  are denoted with subscript  $\gamma$  and are used to assess the scalings of the TTI layers. For examples,  $\eta_\gamma$ ,  $u_{\eta\gamma}$ , and  $\tau_{\eta\gamma}$ , are the Kolmogorov scales calculated in the intermittent regions.

### C. Mean profiles of scalar and vorticity near the TTI layer

Figure 8 shows the conditional averages of passive scalar and vorticity magnitude,  $\langle \phi \rangle_I$  and  $\langle |\omega| \rangle_I = \langle |\nabla \times \mathbf{u}| \rangle_I$ , near the TTI layer bounded by the large- and small-TKE regions at  $t/T_r = 22$ . Here, the interface coordinate  $\zeta_I$  is normalized by the Kolmogorov scale at the center of the shearless mixing layer,  $\eta_C$ . For both large- and small-TKE regions,  $\langle \phi \rangle_I$  significantly varies near  $\zeta_I = 0$ . The profiles of  $\langle \phi \rangle_I$  are similar to the mean scalar profile observed near the TNTI layers.<sup>8,81</sup> The mean vorticity also exhibits a clear jump near the interface:  $\langle |\omega| \rangle_I$  increases from  $\zeta_I = 0$  to the shearless mixing layer ( $\zeta_I < 0$ ). This rapid increase in  $\langle |\omega| \rangle_I$  is observed for  $\zeta_I$  where the jump of  $\langle \phi \rangle_I$  is observed. For the large- and small-TKE regions ( $\zeta_I > 0$ ),  $\langle |\omega| \rangle_I$  gradually increases with  $\zeta_I$ . Although the TKE increases from the small- to large-TKE regions, the vorticity magnitude near the TTI layer does not simply increase according to this relation. A similar observation was reported for a turbulent wake developing in freestream turbulence, where the profile of the vorticity does not match that of velocity variances.<sup>24</sup> Both vorticity and scalar profiles suggest that the shearless mixing layer is separated from the outside by the TTI layer with a small thickness, across which the mean vorticity and scalar rapidly change.

A recent study of the TNTI layer has shown that the mean vorticity magnitude  $\langle |\omega| \rangle_I$  on the interface coordinate collapses well even in different flows and Reynolds numbers when the plots are normalized with the local Kolmogorov scales defined with the mean kinetic energy dissipation rate  $\langle \epsilon \rangle_I$  calculated as a function of  $\zeta_I$ .<sup>15</sup> Here, the Kolmogorov length, velocity, and time scales are defined as  $\eta_I = (\nu^3 / \langle \epsilon \rangle_I)^{1/4}$ ,  $u_{\eta I} = (\nu \langle \epsilon \rangle_I)^{1/4}$ , and  $\tau_{\eta I} = (\nu / \langle \epsilon \rangle_I)^{1/2}$ . Figure 9 plots  $\langle |\omega| \rangle_I / (\tau_{\eta I}^{-1})$  against  $\zeta_I / \eta_I$  for both large- and small-TKE regions at



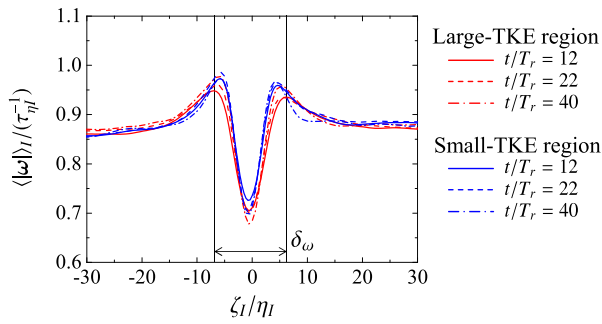


**FIG. 9.** Conditional average of vorticity magnitude  $\langle |\omega| \rangle_I$  normalized by the local Kolmogorov timescale  $\tau_{\eta I}$ . The coordinate  $\zeta_I$  is also normalized by the local Kolmogorov scale  $\eta_I$ . Vertical lines indicate the locations of the local maxima of  $\langle |\omega| \rangle_I$  at  $t/T_r = 12$  for the large-TKE region, which are used to quantify the thickness of the TTI layer,  $\delta_\omega$ .

different times. Although the profiles of  $\langle |\omega| \rangle_I$  are different for the TTI layers of the large- and small-TKE regions in Fig. 8, the plots normalized by the local Kolmogorov scales are almost identical. The normalized vorticity is locally small at  $\zeta_I = 0$  while it attains peaks at  $\zeta_I / \eta_I \approx \pm 6$ . From the definition of  $\tau_{\eta I}$ ,  $\langle |\omega| \rangle_I / \tau_{\eta I}^{-1}$  is rewritten as  $\langle |\omega| \rangle_I / (\langle 2S_{ij}S_{ij} \rangle_I)^{1/2}$ . Therefore, small  $\langle |\omega| \rangle_I / \tau_{\eta I}^{-1}$  at  $\zeta_I = 0$  suggests that the vorticity is relatively weak compared to the strain. On the other hand, the peaks of  $\langle |\omega| \rangle_I / \tau_{\eta I}^{-1}$  at  $\zeta_I / \eta_I \approx \pm 6$  are due to strong vorticity, which can be related to vortex tubes as discussed below. A similar peak was also observed near the TNTI layer, where  $\langle |\omega| \rangle_I / \tau_{\eta I}^{-1}$  increases from 0 to the peak, implying that the TNTI and TTI layers partially comprise a similar internal structure.<sup>15</sup>

The jumps observed for  $\langle \phi \rangle_I$  and  $\langle |\omega| \rangle_I$  in Fig. 8 suggest that the TTI layers of the shearless mixing layer have a finite thickness. The thickness is quantified with the mean scalar profile  $\langle \phi \rangle_I$ . Figure 10 shows the first and second derivatives of  $\langle \phi \rangle_I$  with respect to  $\zeta_I$ , where  $d\langle \phi \rangle_I / d\zeta_I$  and  $d^2\langle \phi \rangle_I / d\zeta_I^2$  are normalized by the maximum values of  $|d\langle \phi \rangle_I / d\zeta_I|$  and  $|d^2\langle \phi \rangle_I / d\zeta_I^2|$ , respectively. Because of the variation of  $\langle \phi \rangle_I$  with  $\zeta_I$ ,  $d\langle \phi \rangle_I / d\zeta_I$  has a large peak within the TTI layer while it hardly depends on  $\zeta_I$  in the shearless mixing layer and the large- and small-TKE regions near the TTI layers. Therefore,  $d^2\langle \phi \rangle_I / d\zeta_I^2$  exhibits positive and negative peaks within the TTI layer and approaches zero as  $|\zeta_I|$  increases. The thickness  $\delta_\phi$  is quantified as a distance between two locations where  $d^2\langle \phi \rangle_I / d\zeta_I^2$  is equal to 5% of the peak value of  $|d^2\langle \phi \rangle_I / d\zeta_I^2|$ , which is shown with horizontal broken lines in Fig. 10.

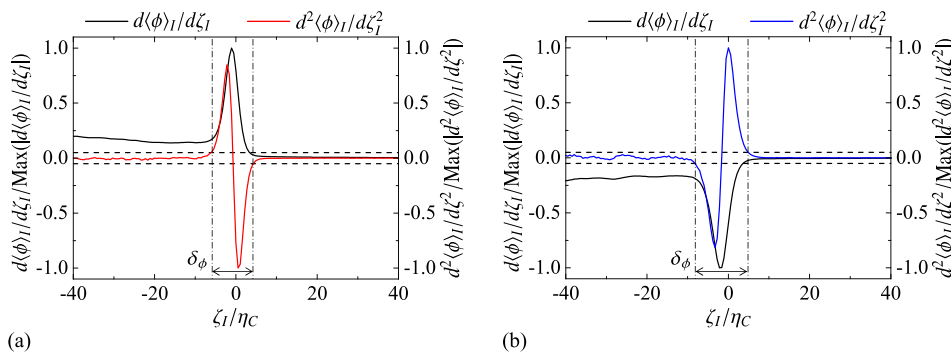


**FIG. 10.** Profiles of  $d\langle \phi \rangle_I / d\zeta_I$  and  $d^2\langle \phi \rangle_I / d\zeta_I^2$  near the TTI layers bounded by (a) the large-TKE region and (b) the small-TKE region. In each figure,  $d\langle \phi \rangle_I / d\zeta_I$  and  $d^2\langle \phi \rangle_I / d\zeta_I^2$  are normalized by the maximum values of  $|d\langle \phi \rangle_I / d\zeta_I|$  and  $|d^2\langle \phi \rangle_I / d\zeta_I^2|$ , respectively. The horizontal broken lines represent 5% of the maximum values of  $|d^2\langle \phi \rangle_I / d\zeta_I^2|$  and are used to define the layer thickness as indicated by the vertical lines.

The layer thickness is also evaluated with the normalized mean vorticity profile  $\langle |\omega| \rangle_I / (\tau_{\eta I}^{-1})$ , following the studies of the TNTI layer,<sup>15</sup> whose thickness is determined with the location of the local maximum of  $\langle |\omega| \rangle_I / (\tau_{\eta I}^{-1})$ . Similarly, the thickness of the TTI layer is estimated as the distance between the local maxima shown in Fig. 9. The thickness obtained with  $\langle |\omega| \rangle_I / (\tau_{\eta I}^{-1})$  is denoted by  $\delta_\omega$ .

Figure 11 shows the temporal variations of the thickness of the TTI layer. The thickness is evaluated for both TTI layers bounded by the large- and small-TKE regions. In Fig. 11(a),  $\delta_\phi / M_1$  and  $\delta_\omega / M_1$  are compared with the Kolmogorov scale  $\eta_C$ . The thickness estimated from the mean vorticity and scalar profiles is close to each other and increases with time. The increase in the thickness is similar to that of the Kolmogorov scale. Figure 11(b) presents the thickness normalized by the Kolmogorov scales in the intermittent region  $\eta_\eta$ . The thickness normalized by the Kolmogorov scale is less dependent on time than  $\delta_\phi / M_1$  and  $\delta_\omega / M_1$ . The thickness is about 12 times the Kolmogorov scales, suggesting that the layer structure is related to the small-scale properties of the shearless mixing layer. This thickness is close to the thickness of the TNTI layer in turbulent free shear flows.<sup>15</sup> The thickness of the TTI layer of about  $12\eta_I$  is similar for grids 1 and 2 and is not directly related to the mesh sizes,  $M_1$  and  $M_2$ . The thickness is expected to be determined by the length scales of the vortical structures within the TTI layer, as explained below. The size of small-scale vortical structures normalized by the Kolmogorov scale hardly depends on flows and Reynolds numbers.<sup>39,82</sup> For the same reason, the thickness of the TNTI layer is determined by  $\eta$  and does not explicitly depend on the global length scale of flows.<sup>15</sup>

## D. The relevance of vortex tubes and sheets to the TTI layer

The internal structure of the TTI layers is examined with the statistics of a velocity gradient tensor  $\partial u_i / \partial x_j$ . The second and third invariants of  $\partial u_i / \partial x_j$  are defined as  $Q = (\omega_i \omega_i - 2S_{ij}S_{ij})/4$  and  $R = -(S_{ij}S_{jk}S_{ki}/3 + \omega_i S_{ij} \omega_j / 4)$ , where  $\omega_i$  is the  $i$ th component of the vorticity vector. Figure 12(a) shows the conditional averages of  $Q$  and  $R$  near the TTI layer. The local Kolmogorov scales are used to normalize  $\langle Q \rangle_I$ ,  $\langle R \rangle_I$ , and  $\zeta_I$ . The profiles are similar for the large- and small-TKE regions and hardly depend on time. Here,  $\langle Q \rangle_I$  is negative for  $|\zeta_I / \eta_I| \lesssim 3$  while positive peaks are observed at  $|\zeta_I / \eta_I| \approx 6$ . An average of  $Q$  is almost zero in turbulent flows if the average is taken as a time or volume average. Therefore,  $\langle Q \rangle_I$  approaches zero for large  $|\zeta_I|$ , where the presence of the TTI layer does not affect the statistics of  $Q$ . Positive  $Q$  is related to the dominance of rotating motions with large

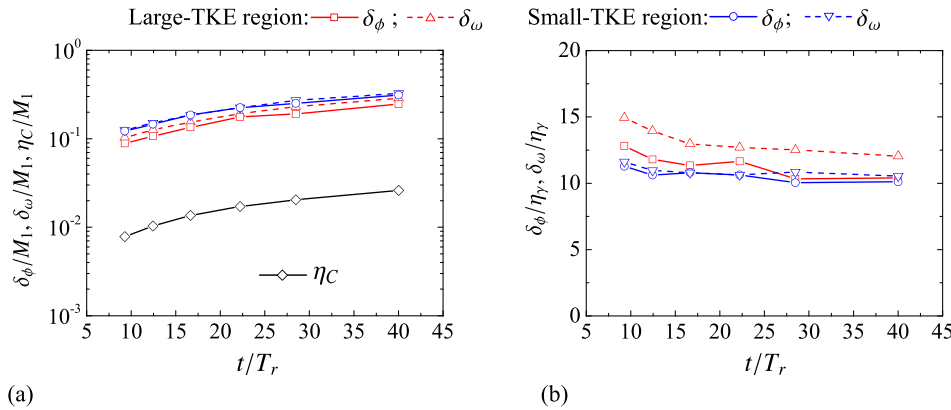


**FIG. 11.** Temporal variations of the thickness of the TTI layers normalized by (a) the mesh size of grid 1,  $M_1$ , and (b) the Kolmogorov scale in the intermittent region,  $\eta_I$ . The thicknesses estimated by mean scalar and mean vorticity magnitude are denoted by  $\delta_\phi$  and  $\delta_\omega$ , respectively. Panel (a) also shows the Kolmogorov scale at the center of the shearless mixing layer,  $\eta_C$ .

$\omega_i \omega_i$  over straining motions and is used to detect vortex tubes in turbulent flows. Therefore, positive  $\langle Q \rangle_I$  at  $|\zeta_I/\eta_I| \approx 6$  implies that vortex tubes are frequently observed. Since the thickness of the TTI layer is about 12 times the Kolmogorov scale,  $|\zeta_I/\eta_I| \approx 6$  is close to the edges of the TTI layer. Thus, the TTI layer is formed in the vicinity of the vortex tubes. The variation of  $\langle R \rangle_I$  with  $\zeta_I$  is anti-correlated with that of  $\langle Q \rangle_I$ :  $\langle R \rangle_I$  have positive and negative peaks at  $|\zeta_I/\eta_I| \approx 0$  and 6, respectively. The governing equations of  $S_{ij}S_{ij}$  and  $\omega_i \omega_i/2$  contain the production terms written as  $-S_{ij}S_{jk}S_{ki}$  and  $\omega_i S_{ij} \omega_j$ , respectively. Therefore, the profile of  $R = -(S_{ij}S_{jk}S_{ki}/3 + \omega_i S_{ij} \omega_j/4)$  indicates that the enstrophy production is dominant over the strain amplification at  $|\zeta_I/\eta_I| \approx 6$  while the strain production is significant near the center of the TTI layer ( $\zeta_I/\eta_I \approx 0$ ).

Figure 12(b) shows the trajectory of  $(\langle R \rangle_I, \langle Q \rangle_I)$  across the TTI layer bounded by the large-TKE region. The same result is also obtained for the small-TKE region. The locations of  $\zeta_I/\eta_I = 0, \pm 3, \pm 5$ , and  $\pm 10$  are marked on the trajectory as A, B $\pm$ , C $\pm$ , and D $\pm$ , respectively. The black solid line is the discriminant of the eigenvalues of  $\partial u_i/\partial x_j$ , which is written as  $D = (27/4)R^2 + Q^3 = 0$ . The isosurface used to identify the TTI layer is located at  $\zeta_I = 0$  (A), near which the maximum value of  $\langle R \rangle_I$  and the minimum value of  $\langle Q \rangle_I$  are observed. As  $|\zeta_I|$  increases for both positive and negative  $\zeta_I$ , the plot of  $(\langle R \rangle_I, \langle Q \rangle_I)$  moves toward the second quadrant, where  $\langle Q \rangle_I$  reaches the maximum near  $\zeta_I/\eta_C = \pm 5$  (C $\pm$ ). Then,  $(\langle R \rangle_I, \langle Q \rangle_I)$  further approaches (0, 0). The trajectory of  $(\langle R \rangle_I, \langle Q \rangle_I)$  has also been

investigated for the TNTI layer in previous studies.<sup>41,46</sup> Two sublayers are known as the internal layers of the TNTI layer: the viscous superlayer, where the growth of enstrophy is dominated by viscous diffusion; the turbulent sublayer, where vortex stretching is as important as viscous effects.<sup>13,38</sup> Here, the non-turbulent region near the TNTI layer is known to have negligibly small enstrophy ( $\omega_i \omega_i/2 = 0$ ) and small but finite strain rate ( $S_{ij}S_{ij} > 0$ ) while the turbulent core region exhibits its velocity statistics of fully developed turbulence.<sup>46</sup> The viscous superlayer forms at the outer edge of the TNTI layer, which is bounded by a non-turbulent region. The turbulent sublayer is a buffer layer that forms between the viscous superlayer and a turbulent core region. The trajectory of  $(\langle R \rangle_I, \langle Q \rangle_I)$  from the viscous superlayer toward the turbulent core region across the turbulent sublayer is approximately represented by a straight line from the fourth quadrant with  $\langle R \rangle_I > 0$  and  $\langle Q \rangle_I < 0$  toward the second quadrant with  $\langle R \rangle_I < 0$  and  $\langle Q \rangle_I > 0$ .<sup>41,46</sup> This trajectory across the turbulent sublayer is similar to the present results for the TTI layer. In addition,  $\langle Q \rangle_I$  normalized by the local Kolmogorov scales near the TNTI layer also exhibits a positive peak with  $\langle Q \rangle_I/\tau_{\eta I}^{-2} = 0.05$ – $0.07$  near the boundary between the turbulent sublayer and the turbulent core region.<sup>15</sup> This peak value is quantitatively consistent with the peaks of  $\langle Q \rangle_I/\tau_{\eta I}^{-2}$  for the TTI layer in Fig. 12(a). The peaks are observed at  $\zeta_I/\eta_I \approx \pm 6$ , which are close to the boundaries between the TTI layers and the large- or small-TKE region. Thus, the peaks in  $\langle Q \rangle_I/\tau_{\eta I}^{-2}$  appear at the boundaries of the TTI or TNTI layer from adjacent turbulent regions. These

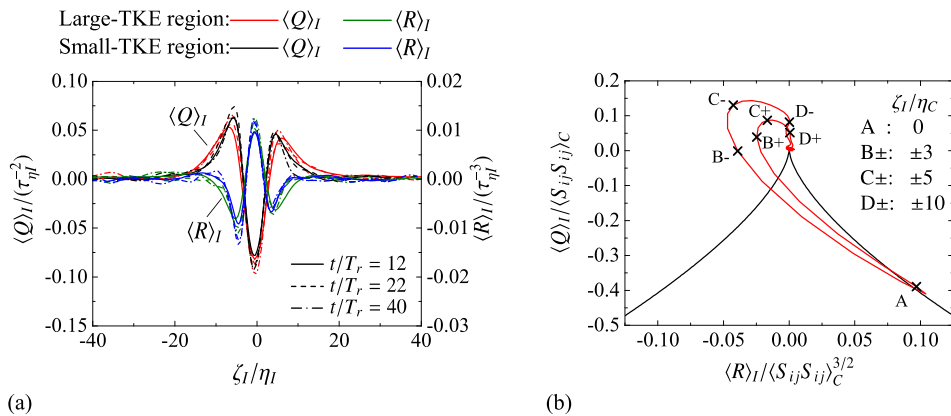


**FIG. 12.** (a) Conditional averages of the second and third invariants of a velocity gradient tensor,  $\langle Q \rangle_I$  and  $\langle R \rangle_I$ , near the TTI layers. The plots are normalized by the local Kolmogorov scales  $\tau_{\eta I}$  and  $\eta_I$ . (b) The trajectory of  $(\langle Q \rangle_I, \langle R \rangle_I)$  from  $\zeta_I/\eta_I = -40$  to 40 for the TTI layer bounded by the large-TKE region at  $t/T_r = 22$ .

comparisons imply a similar internal structure of the TTI layer to that of the turbulent sublayer.

The analysis of shearing and rotating motions within the TNTI layer has also suggested that the outer edge of the turbulent sublayer bounded by the viscous superlayer is characterized by intense shear while rotating motions become important at the inner edge bounded by the turbulent core region.<sup>66</sup> The shearing motion is attributed to the existence of vortex sheets, which are thin layers with intense shear, while the rotating motion is due to vortex tubes.<sup>41,66</sup> The conditional statistics of  $Q$  also suggest that the edge of the TTI layer is dominated by vortex tubes, whose distance from the center of the TTI layer is expected to be about  $6\eta$ , at which  $\langle Q \rangle_I / \tau_{\eta}^{-2}$  has positive peaks. The relevance of vortex sheets to the TTI layer is further investigated here. The second-order velocity gradient tensor  $A_{ij} = S_{ik}\Omega_{kj} + S_{jk}\Omega_{ki}$  ( $\Omega_{ij}$ : a rate-of-rotation tensor) is often used to identify vortex sheets, whose detector function can be defined as  $D_S \equiv \sqrt{A_{ij}A_{ji}/2}$  because of large  $D_S$  within the vortex sheets.<sup>83–86</sup> Figure 13 shows the conditional average of  $\langle D_S \rangle_I$  near the TTI layer for the large-TKE region. A peak of  $\langle D_S \rangle_I$  is observed at  $\zeta_I \approx 0$ . Negative  $\langle Q \rangle_I$  and large  $\langle D_S \rangle_I$  at  $\zeta_I \approx 0$  indicate that the dominant vortical structures within the TTI layer are the vortex sheets rather than vortex tubes. Studies of vortex sheets in turbulence have confirmed that the vortex sheets appear in the vicinity of vortex tubes, whose rotating motion sustains intense shear within the vortex sheets.<sup>78</sup> The local maxima of  $\langle Q \rangle_I$  observed at  $|\zeta_I/\eta| \approx 6$  in Fig. 12(a) agrees with this configuration of vortex tubes and vortex sheets.

The alignment between the TTI layer and these vortical structures is examined with the angle  $\theta_{\phi\omega}$  between the interface-normal direction  $\mathbf{n}_\phi$  and the vorticity direction  $\mathbf{n}_\omega = \boldsymbol{\omega}/|\boldsymbol{\omega}|$ . Figure 14 shows the probability density function (PDF) of  $\cos \theta_{\phi\omega} = \mathbf{n}_\phi \cdot \mathbf{n}_\omega$  near the TTI layer bounded by the large-TKE region. Here,  $\mathbf{n}_\phi$  for the large-TKE region is defined as  $\mathbf{n}_\phi = \nabla \phi / |\nabla \phi|$ , by which  $\mathbf{n}_\phi$  points in the outward direction of the shearless mixing layer. The interface orientation  $\mathbf{n}_\phi$  is evaluated at  $\zeta_I = 0$  while the vorticity direction  $\mathbf{n}_\omega$  is taken at various locations on  $\zeta_I$ . A large peak is observed for  $\cos \theta_{\phi\omega} = 0$  at  $\zeta_I/\eta_C = 0$ , suggesting that the vorticity vector of the vortex sheets is mostly perpendicular to the interface orientation. In addition, the peak at  $\cos \theta_{\phi\omega} = 0$  is also observed at  $\zeta_I/\eta_C = \pm 3$  and  $\pm 5$ , where the probability tends to be lower as  $|\cos \theta_{\phi\omega}|$  increases. Thus, the vorticity vector within the TTI layer ( $|\zeta_I/\eta| \lesssim 6$ ) also tends to be perpendicular

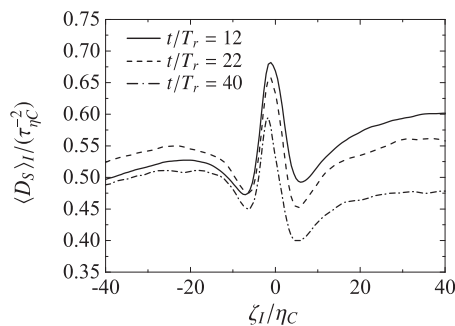


**FIG. 13.** Conditional average of the detector function of vortex sheets,  $D_S \equiv \sqrt{A_{ij}A_{ji}/2}$  ( $A_{ij} = S_{ik}\Omega_{kj} + S_{jk}\Omega_{ki}$ ), near the TTI layer bounded by the large-TKE region.

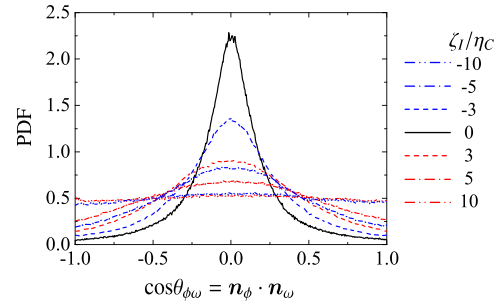


**FIG. 14.** Probability density function of  $\cos \theta_{\phi\omega} = \mathbf{n}_\phi \cdot \mathbf{n}_\omega$  for the TTI layer bounded by the large-TKE region at  $t/T_r = 22$ . Here, the interface normal direction  $\mathbf{n}_\phi$  is evaluated at  $\zeta_I = 0$  while the vorticity direction  $\mathbf{n}_\omega$  is taken at different locations on  $\zeta_I$ .

to the interface orientation. This alignment indicates that the vortex sheets and tubes within the TTI layer are parallel to the interface. At  $\zeta_I/\eta = \pm 10$ , the PDF has a flat shape, and no preference of the vorticity direction with respect to the interface orientation is found at this location. Therefore, as also found for  $\langle Q \rangle_I \approx 0$  at large  $|\zeta_I|$ , small-scale turbulent motions far from the TTI layer are hardly influenced by the presence of the TTI layer.

The vortex sheets in turbulent flows have a thickness that scales with the Kolmogorov scale.<sup>87,88</sup> The small thickness of the vortex sheets is sustained by compressive strain acting in the direction perpendicular to the sheets.<sup>87</sup> This mechanism to sustain the thin layer should be relevant to the thickness of the TTI layer, where the vortex sheets are prominent as suggested by large  $\langle D_S \rangle_I$ . Since the TTI layer in the shearless mixing layer tends to face the inhomogeneous ( $z$ ) direction, the  $z$ -directional velocity  $w$  is related to the compressive strain acting on the vortex sheets within the TTI layer. Figure 15(a) shows the conditional average of  $w$ ,  $\langle w \rangle_I$ , which exhibits a Z-shaped distribution across the TTI layer. A similar profile has been reported for the mean velocity profile across vortex sheets in turbulence.<sup>87</sup> Positive  $\langle w \rangle_I$  for  $\zeta_I < 0$  and negative  $\langle w \rangle_I$  for  $\zeta_I > 0$  suggest that the TTI layer is subject to the compressive strain in the layer-normal direction. Positive and negative peaks are observed for  $\langle w \rangle_I$ . The difference between these peak values is denoted by  $\Delta w_I$ . Figure 15(b) shows the temporal variation of  $\Delta w_I$  normalized by the Kolmogorov velocity scale in the intermittent region,  $u_{\eta\gamma}$ . For both TTI layers bounded by the large- and small-TKE regions,  $\Delta w_I/u_{\eta\gamma}$  hardly depends on time. Therefore, the velocity jump across the TTI layer scales with the Kolmogorov scale. In addition,  $\Delta w_I$  normalized by the Kolmogorov scale is 3–4, which is quantitatively consistent with the velocity jump observed near the vortex sheets in turbulence with a wide range of the turbulent Reynolds number.<sup>87</sup> In Fig. 15(a), the mean velocity jump is observed over a distance of about  $20\eta$ , which is close to the length of the compressive-strain field observed near vortex sheets in turbulent planar jets and isotropic turbulence.<sup>82</sup> Thus, the entire TTI layer with a thickness of about  $12\eta$  is influenced by the compressive strain.

The results presented above have indicated that the TTI layers appear along the vortex sheets, which are formed in the vicinity of the vortex tubes. Figure 16 illustrates the structure of the TTI layer based on the conditional statistics. The configuration between the vortex

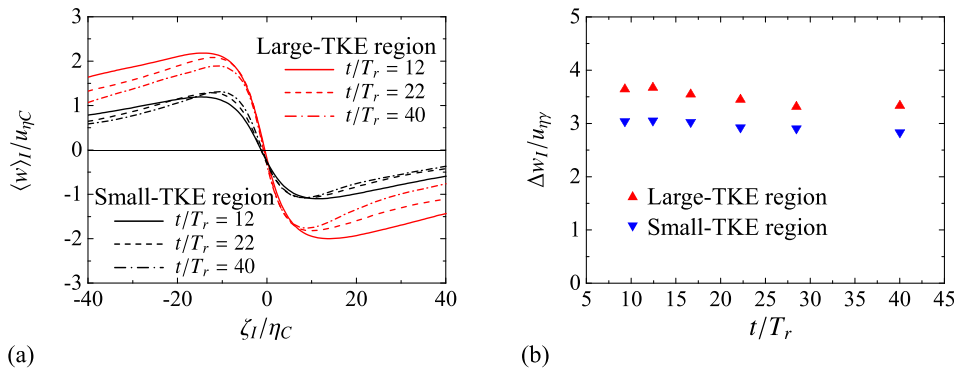


**FIG. 15.** (a) Conditional average of  $w$  near the TTI layers for the large- and small-TKE regions. (b) Temporal variation of the velocity jump  $\Delta w_I$  of  $\langle w \rangle_I$  normalized by the Kolmogorov velocity scale  $u_{\eta}$ .

sheets and vortex tubes has been investigated in turbulent flows,<sup>78</sup> where two vortex tubes, on average, appear on the sides of a vortex sheet. In addition, previous studies of these structures have shown that the diameter of the vortex tubes,  $d_T$ , is about  $8\eta$  while the thickness of the vortex sheets,  $\delta_S$ , is about  $4\eta$ .<sup>66,87–90</sup> The sketch in Fig. 16 is based on these observations of the vortex tubes and sheets and the conditional statistics for the TTI layer. The local maximum of  $D_S \equiv \sqrt{A_{ij}A_{ji}}/2$  at  $\zeta_I = 0$  confirms that the center of the TTI layer is mostly occupied by the vortex sheets with large  $D_S$  and negative  $Q$ . The vortex sheets are thinner than the TTI layer, whose thickness is about  $\delta_\phi = 12\eta$ . The peak locations of  $\langle Q \rangle_I$  suggest that the center of the vortex tubes is located near the boundaries that separate the TTI layer from the shearless mixing layer or the large/small-TKE region. Therefore, the TTI layer consists of vortex tubes and sheets, both of which affect the conditional statistics near the TTI layer. The arrows shown inside the vortex tubes and vortex sheets indicate the velocity induced by these structures, which is based on the analysis of vortex tubes and sheets in Ref. 78. It was shown that the vortex tubes besides the vortex sheet induce a flow toward the vortex sheet.<sup>78</sup> This velocity toward the vortex sheet is observed as positive and negative  $\langle w \rangle_I$  on  $\zeta_I < 0$  and  $\zeta_I > 0$ , respectively, near the TTI layer, as illustrated with thick arrows in Fig. 16. The vortex sheets have a finite aspect ratio, and their spatial distribution is intermittent. Therefore, the origin of the interface coordinate  $\zeta_I = 0$  is not always located within the vortex sheets. In addition,  $\zeta_I$  does not always intersect the vortex tubes besides the vortex sheets. However, the probability to observe the vortex sheets at  $\zeta_I = 0$  and the vortex tubes at  $|\zeta_I/\eta| \approx 6$  is relatively high compared with that to observe these structures far away from the TTI layer. Therefore, these configurations of the vortex tubes and sheets explain well the conditional statistics near the TTI layer.

### E. The development of the shearless turbulence mixing layer

The development of the shearless turbulence mixing layer is investigated with the characteristics of the TTI layer. Following the entrainment analysis of turbulent free shear flows, the local entrainment velocity  $v_n$  is defined with the propagation velocity of the isosurface used to detect the TTI layer.<sup>5</sup> The propagation velocity of the isosurface of  $\phi$  relative to fluid motion is denoted as  $v_n$ . Here,  $v_n$  is interpreted as a fluid volume that is entrained into the shearless mixing layer from the outside per a unit surface area of the interface and per a unit time. Positive  $v_n$  represents the entrainment from the outside into the shearless mixing layer while negative  $v_n$  indicates that the fluid in the shearless mixing layer is left outside. For this definition,  $v_n$  is calculated as  $v_n = -(D\phi/Dt)/|\nabla\phi|$  and  $(D\phi/Dt)/|\nabla\phi|$  for the interfaces bounded by the large- and small-TKE regions, respectively.<sup>91</sup> Figure 17 shows the PDF of  $v_n$  normalized by  $U_0$  or  $u_{\eta}$ . The PDF of  $v_n/U_0$  has a narrower distribution at a later time, and the magnitude of  $v_n/U_0$  becomes smaller. On the other hand, the PDF of  $v_n/u_{\eta}$  weakly depends on time, and the entrainment velocity is related to the Kolmogorov velocity. The PDF of  $v_n$  suggests that  $v_n$  tends to be positive and the fluid is entrained into the shearless mixing layer.

The total entrainment rate depends on the surface area of the interface as well as the local entrainment velocity and can be evaluated as the surface integral of  $v_n$  on the isosurface of  $\phi$ . Figure 18(a) shows the non-dimensional surface area  $\hat{S} = S/L_x L_y$ , where  $S$  is the area of the scalar isosurface used to detect the TTI layer. The isosurface of  $\phi$  may detect small bubble-like regions of large- or small-TKE regions inside the shearless mixing layer. These bubble-like regions have slightly larger or smaller values of  $\phi$  than the shearless mixing layer and are surrounded by the shearless mixing layer. The isosurface

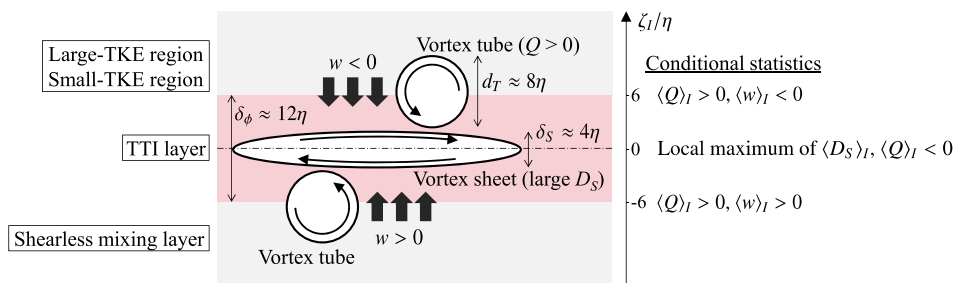


**FIG. 16.** A schematic of the structure of the TTI layer indicated by conditional statistics.



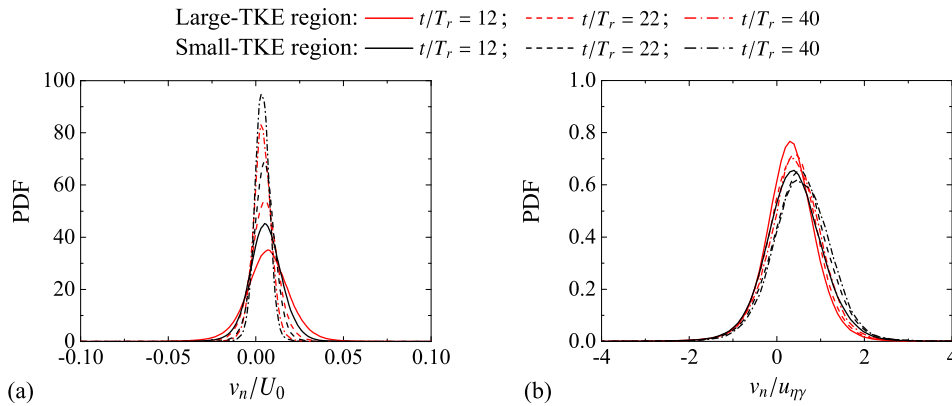


FIG. 17. The probability density function of the local entrainment velocity  $v_n$  normalized by (a)  $U_0$  and (b)  $u_{\eta\gamma}$ .

associated with the bubble-like regions does not separate the shearless mixing layer from the outsides. Therefore, these regions are not considered in calculating the surface area. When the isosurface of  $\phi$  is visualized, several independent isosurfaces are observed in each snapshot of the flow. The surface area is evaluated as the area of the largest isosurface, which does not contain the contribution from the bubbles. For both large- and small-TKE regions,  $\hat{S}$  decreases with time. In addition, the large-TKE region has a larger  $\hat{S}$  than the small-TKE region. The scalar isosurface has a complicated geometry that is influenced by large- and small-scales of turbulent motions,<sup>92</sup> as also shown in Fig. 6. Therefore, the surface area strongly depends on the Reynolds number. As the Reynolds number increases, the scale separation between large and small scales becomes larger and the surface area increases. This was also confirmed for the scalar isosurface in a turbulent mixing layer, where the area of the scalar isosurface increases by the flow development accompanied by the increase in the integral and turbulent Reynolds numbers.<sup>93</sup> The surface area of the interface of the shearless mixing layer also shows the same Reynolds number dependence. The surface area decreases with time because of the decay of  $Re_\lambda$  in Fig. 3. In addition,  $Re_\lambda$  decreases from the large-TKE to the small-TKE regions. This explains the smaller surface area for the interface for the small-TKE region than that for the large-TKE region. Blakeley *et al.* investigated the evolution of scalar isosurfaces in decaying homogeneous, isotropic turbulence, where the initial scalar profile was provided by a hyperbolic tangent function as also done in the present DNS.<sup>94</sup> They observed that the surface areas with low and high thresholds used for detecting the TTI layers in this study decrease with

time at a late time. This decreasing trend is also consistent with the decay of  $\hat{S}$  in the shearless mixing layer even though the shearless mixing layer is not homogeneous in the  $z$  direction. The decrease in the surface area observed in decaying isotropic turbulence is due to molecular diffusion, which has destructive effects on the surface area.<sup>94</sup>

The entrainment rate  $Q_E$  is evaluated as the surface integral of  $v_n$  over the isosurface of  $\phi$  used to detect the TTI layer. Figure 18(b) shows the temporal variation of  $Q_E$  for the large- and small-TKE regions. The interface of the large-TKE region has larger  $Q_E$  than that of the small-TKE region. This difference is attributed to the larger surface area for the interface of the large-TKE region in Fig. 18(a). The vertical profiles of velocity variance suggested that the shearless mixing layer spatially expands with time.<sup>35</sup> Consistently,  $Q_E > 0$  also confirms that the fluid in the large- and small-TKE regions is entrained into the shearless mixing layer. The difference in  $Q_E$  between the large- and small-TKE regions suggests that the entrainment from the large-TKE region has a larger contribution to this growth of the shearless mixing layer than that from the small-TKE region. Large-scale vortices from the large-TKE region often penetrate the shearless mixing layer, where the large-scale intermittency is more significant than in the other regions.<sup>42</sup> The penetration of the large-scale vortices can contort the TTI layer and contributes to the large surface area for the large-TKE region. This large-scale intermittency may also affect a higher entrainment rate from the large-TKE region. Consistently, experiments of a turbulent jet issued into homogeneous isotropic turbulence have suggested that the interface of the jet is significantly contorted

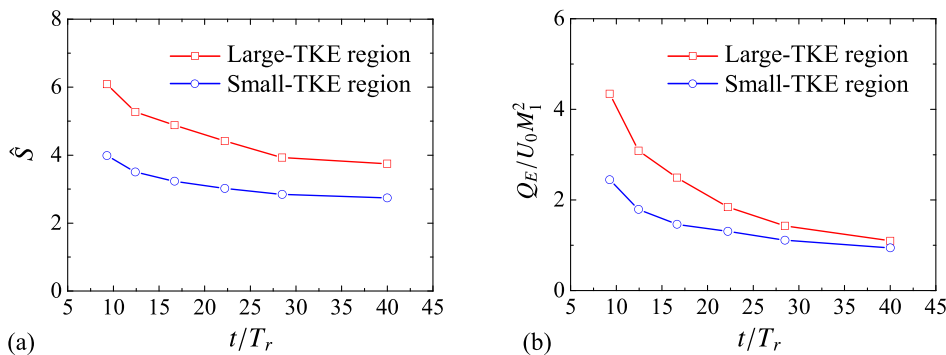


FIG. 18. Temporal variations of (a) the surface area  $S$  of the isosurface of  $\phi$  normalized by  $L_x L_y$  and (b) the total entrainment rate  $Q_E$  evaluated with the surface integral of the local entrainment velocity. The results are compared for the TTI layers bounded by the large- and small-TKE regions.

under the influence of external turbulence.<sup>95</sup> A similar influence of large-scale vortices is also reported for the TNTI layer, whose contorted geometry can be explained by the large-scale vortices that cause engulfment.<sup>96</sup>

#### IV. CONCLUSION

The TTI layers that form at the edges of the shearless turbulence mixing layer have been investigated with DNS of temporally evolving grid turbulence. The present study has considered the parallel-bar grid with two different mesh sizes following the wind tunnel experiment in Ref. 35. The flow comprises three turbulent regions: two regions of quasi homogeneous isotropic turbulence generated by the grids and the shearless turbulence mixing layer between them. These regions have been successfully identified from a passive scalar field, and the scalar isosurface has been used to identify the TTI layers. The present study has adapted the conditional averages, which calculate the statistics as functions of a position with respect to the TTI layer.

The conditional averages of passive scalar and vorticity magnitude exhibit a distinct jump within the TTI layer, which confirms a clear separation by the TTI layer between the shearless mixing layer and the outside. Although the thickness of the TTI layer increases with time as turbulence decays, the thickness normalized by the Kolmogorov scale stays at about 12, which is close to the thickness of the TNTI layer in turbulent free shear flows and boundary layers. The internal structure of the TTI layer has been examined with the conditional statistics of a velocity gradient tensor  $\partial u_i / \partial x_j$ . The mean vorticity profile normalized by the local Kolmogorov scale has a universal shape that is independent of time and hardly differs for the interfaces bounded by the large- and small-TKE regions. The conditional averages of the vorticity magnitude and the second and third invariants of  $\partial u_i / \partial x_j$  suggest that vorticity is more significant than strain at the edges of the TTI layer while the center of the TTI layer is strain dominant. The conditional average of the detector function of vortex sheets has a local maximum within the TTI layer. These profiles of the conditional statistics indicate that the typical vortical structures are vortex sheets and vortex tubes at the center and edges of the TTI layer, respectively. Positive peaks of  $\langle Q \rangle_I$  also indicate that the distance between the vortex tubes from the center of the shear layer is about  $6\eta$ . Since the thickness of the TTI layer is about  $12\eta$ , vortex tubes frequently appear at the boundaries between the TTI layer and adjacent turbulent region. Similarly, the peak of  $\langle Q \rangle_I$  near the TNTI layer was also observed at the boundary between the TNTI layer and turbulent core region.<sup>15</sup> In addition, the peak of  $\langle Q \rangle_I$  normalized by the local Kolmogorov scale is about 0.06 for both TTI and TNTI layers.<sup>15</sup> A recent study of the TNTI layer has also suggested that vortex tubes and sheets exist in the turbulent sublayer, which is an internal layer within the TNTI layer.<sup>66</sup> In addition, the conditional mean trajectory of the second and third invariants of  $\partial u_i / \partial x_j$  is found to be similar between the TTI layer and the turbulent sublayer. These results suggest that the internal structure of the TTI layer resembles that of the turbulent sublayer. The presence of vortex sheets in the vicinity of vortex tubes within the TTI layer is consistent with the interaction between vortex sheets and tubes observed in isotropic turbulence.<sup>78</sup> The configuration of these vortical structures also explains a compressive strain within the TTI layer, which is caused by the flow toward the TTI layer in the layer-normal direction. The mean velocity jump associated with the compressive strain across the TTI layer is about  $3u_\eta$  while this

jump is observed over a distance of about  $20\eta$ , which is larger than the thickness of the TTI layer. These values are consistent with the velocity jump and its width for the compressive strain of vortex sheets,<sup>82</sup> implying that the characteristics of vortex sheets strongly affect the flow field around the TTI layer.

The development of the shearless mixing layer has also been studied with the local entrainment rate, which is defined as the propagation velocity of the scalar isosurface used to identify the TTI layer. Although the velocity scale of the shearless mixing layer varies with time, the local entrainment rate normalized by the Kolmogorov velocity hardly depends on time. The surface area of the isosurface tends to be small with the decrease in the turbulent Reynolds number. Because of the difference in the surface area between the TTI layers bounded by the large- and small-TKE regions, the shearless mixing layer entrains more amount of fluid from the large-TKE region than from the small-TKE regions. These results for the internal structure and the entrainment of the TTI layer will be useful for constructing the physical models in future studies possibly as an extension of the models proposed for the TNTI layers.

#### ACKNOWLEDGMENTS

Numerical simulations were performed using the high-performance computing system of the Japan Agency for Marine–Earth Science and Technology. This work was also supported by the Collaborative Research Project on Computer Science with High-Performance Computing in Nagoya University and by JSPS KAKENHI Grant Nos. 20H05754, 22H01398, and 22K03903.

#### AUTHOR DECLARATIONS

##### Conflict of interest

The authors have no conflicts to disclose.

#### Author Contributions

**Kohtaro Nakamura:** Data curation (lead); Formal analysis (lead); Investigation (lead); Methodology (equal); Software (equal); Validation (lead); Visualization (lead); Writing – original draft (supporting); Writing – review & editing (supporting). **Tomoaki Watanabe:** Conceptualization (equal); Data curation (supporting); Formal analysis (supporting); Funding acquisition (equal); Investigation (supporting); Methodology (equal); Project administration (equal); Resources (lead); Software (equal); Supervision (equal); Validation (supporting); Visualization (supporting); Writing – original draft (lead); Writing – review & editing (lead). **Koji Nagata:** Conceptualization (equal); Formal analysis (supporting); Funding acquisition (equal); Investigation (supporting); Methodology (equal); Project administration (equal); Resources (supporting); Supervision (equal); Validation (supporting); Writing – review & editing (equal).

#### DATA AVAILABILITY

The data that support the findings of this study are available from the corresponding author upon reasonable request.

#### REFERENCES

1. S. B. Pope, *Turbulent Flows* (Cambridge University Press, 2000).

- <sup>2</sup>R. O. Fox, *Computational Models for Turbulent Reacting Flows* (Cambridge University Press, 2003).
- <sup>3</sup>W. D. Smyth and J. N. Moum, "Ocean mixing by Kelvin–Helmholtz instability," *Oceanography* **25**, 140 (2012).
- <sup>4</sup>C. B. da Silva, J. C. R. Hunt, I. Eames, and J. Westerweel, "Interfacial layers between regions of different turbulence intensity," *Annu. Rev. Fluid Mech.* **46**, 567 (2014).
- <sup>5</sup>M. Holzner and B. Lüthi, "Laminar superlayer at the turbulence boundary," *Phys. Rev. Lett.* **106**, 134503 (2011).
- <sup>6</sup>D. Mistry, J. Philip, J. R. Dawson, and I. Marusic, "Entrainment at multi-scales across the turbulent/non-turbulent interface in an axisymmetric jet," *J. Fluid Mech.* **802**, 690 (2016).
- <sup>7</sup>T. Watanabe, C. B. da Silva, Y. Sakai, K. Nagata, and T. Hayase, "Lagrangian properties of the entrainment across turbulent/non-turbulent interface layers," *Phys. Fluids* **28**, 031701 (2016).
- <sup>8</sup>J. Westerweel, C. Fukushima, J. M. Pedersen, and J. C. R. Hunt, "Momentum and scalar transport at the turbulent/non-turbulent interface of a jet," *J. Fluid Mech.* **631**, 199 (2009).
- <sup>9</sup>A. Attili, J. C. Cristancho, and F. Bisetti, "Statistics of the turbulent/non-turbulent interface in a spatially developing mixing layer," *J. Turbul.* **15**, 555 (2014).
- <sup>10</sup>D. Krug, M. Holzner, B. Lüthi, M. Wolf, W. Kinzelbach, and A. Tsinober, "The turbulent/non-turbulent interface in an inclined dense gravity current," *J. Fluid Mech.* **765**, 303 (2015).
- <sup>11</sup>T. S. Silva and C. B. da Silva, "The behaviour of the scalar gradient across the turbulent/non-turbulent interface in jets," *Phys. Fluids* **29**, 085106 (2017).
- <sup>12</sup>K. F. Kohan and S. Gaskin, "The effect of the geometric features of the turbulent/non-turbulent interface on the entrainment of a passive scalar into a jet," *Phys. Fluids* **32**, 095114 (2020).
- <sup>13</sup>M. van Reeuwijk and M. Holzner, "The turbulence boundary of a temporal jet," *J. Fluid Mech.* **739**, 254 (2014).
- <sup>14</sup>D. K. Bisset, J. C. R. Hunt, and M. M. Rogers, "The turbulent/non-turbulent interface bounding a far wake," *J. Fluid Mech.* **451**, 383 (2002).
- <sup>15</sup>M. Zecchetto and C. B. da Silva, "Universality of small-scale motions within the turbulent/non-turbulent interface layer," *J. Fluid Mech.* **916**, A9 (2021).
- <sup>16</sup>R. Jahanbakhshi, N. S. Vaghefi, and C. K. Madnia, "Baroclinic vorticity generation near the turbulent/non-turbulent interface in a compressible shear layer," *Phys. Fluids* **27**, 105105 (2015).
- <sup>17</sup>T. Watanabe, X. Zhang, and K. Nagata, "Turbulent/non-turbulent interfaces detected in DNS of incompressible turbulent boundary layers," *Phys. Fluids* **30**, 035102 (2018).
- <sup>18</sup>S. Li, Y. Long, and J. Wang, "Turbulent/non-turbulent interface for laminar boundary flow over a wall-mounted fence," *Phys. Fluids* **34**, 125113 (2022).
- <sup>19</sup>Y. Long, J. Wang, and J. Wang, "'Turbulent/non-turbulent interface' in a low-Reynolds-number transitional boundary layer over a multi-element airfoil," *Phys. Fluids* **34**, 102111 (2022).
- <sup>20</sup>X. Wu, J. M. Wallace, and J.-P. Hickey, "Boundary layer turbulence and free-stream turbulence interface, turbulent spot and freestream turbulence interface, laminar boundary layer and freestream turbulence interface," *Phys. Fluids* **31**, 045104 (2019).
- <sup>21</sup>H. C. Ghimire and S. C. C. Bailey, "An experimental investigation of wing-tip vortex decay in turbulence," *Phys. Fluids* **29**, 037108 (2017).
- <sup>22</sup>K. S. Kankanwadi and O. R. H. Buxton, "Turbulent entrainment into a cylinder wake from a turbulent background," *J. Fluid Mech.* **905**, A35 (2020).
- <sup>23</sup>R. Maryami, S. A. Showkat A, M. Azarpeyvand, and A. Afshari, "Turbulent flow interaction with a circular cylinder," *Phys. Fluids* **32**, 015105 (2020).
- <sup>24</sup>K. S. Kankanwadi and O. R. H. Buxton, "On the physical nature of the turbulent/turbulent interface," *J. Fluid Mech.* **942**, A31 (2022).
- <sup>25</sup>K. F. Kohan and S. J. Gaskin, "On the scalar turbulent/turbulent interface of axisymmetric jets," *J. Fluid Mech.* **950**, A32 (2022).
- <sup>26</sup>J. C. R. Hunt, I. Eames, and J. Westerweel, "Mechanics of inhomogeneous turbulence and interfacial layers," *J. Fluid Mech.* **554**, 499 (2006).
- <sup>27</sup>M. Wolf, M. Holzner, B. Lüthi, D. Krug, W. Kinzelbach, and A. Tsinober, "Effects of mean shear on the local turbulent entrainment process," *J. Fluid Mech.* **731**, 95 (2013).
- <sup>28</sup>T. Watanabe, C. B. da Silva, K. Nagata, and Y. Sakai, "Geometrical aspects of turbulent/non-turbulent interfaces with and without mean shear," *Phys. Fluids* **29**, 085105 (2017).
- <sup>29</sup>T. Watanabe, Y. Sakai, K. Nagata, Y. Ito, and T. Hayase, "Reactive scalar field near the turbulent/non-turbulent interface in a planar jet with a second-order chemical reaction," *Phys. Fluids* **26**, 105111 (2014).
- <sup>30</sup>M. Holzner, B. Lüthi, A. Tsinober, and W. Kinzelbach, "Acceleration, pressure and related quantities in the proximity of the turbulent/non-turbulent interface," *J. Fluid Mech.* **639**, 153 (2009).
- <sup>31</sup>G. H. Good, S. Gershchenko, and Z. Warhaft, "Intermittency and inertial particle entrainment at a turbulent interface: The effect of the large-scale eddies," *J. Fluid Mech.* **694**, 371 (2012).
- <sup>32</sup>S. Veeravalli and Z. Warhaft, "The shearless turbulence mixing layer," *J. Fluid Mech.* **207**, 191 (1989).
- <sup>33</sup>H. S. Kang and C. Meneveau, "Experimental study of an active grid-generated shearless mixing layer and comparisons with large-eddy simulation," *Phys. Fluids* **20**, 125102 (2008).
- <sup>34</sup>M. Kamruzzaman, L. Djenidi, and R. A. Antonia, "Study of the interaction of two decaying grid-generated turbulent flows," *Phys. Fluids* **33**, 095122 (2021).
- <sup>35</sup>T. Matsushima, K. Nagata, and T. Watanabe, "Wavelet analysis of shearless turbulent mixing layer," *Phys. Fluids* **33**, 025109 (2021).
- <sup>36</sup>S. Gershchenko, G. Good, and Z. Warhaft, "Entrainment and mixing of water droplets across a shearless turbulent interface with and without gravitational effects," *J. Fluid Mech.* **668**, 293 (2011).
- <sup>37</sup>J. Westerweel, C. Fukushima, J. M. Pedersen, and J. C. R. Hunt, "Mechanics of the turbulent/non-turbulent interface of a jet," *Phys. Rev. Lett.* **95**, 174501 (2005).
- <sup>38</sup>R. R. Taveira and C. B. da Silva, "Characteristics of the viscous superlayer in shear free turbulence and in planar turbulent jets," *Phys. Fluids* **26**, 021702 (2014).
- <sup>39</sup>C. B. da Silva, R. J. N. Dos Reis, and J. C. F. Pereira, "The intense vorticity structures near the turbulent/non-turbulent interface in a jet," *J. Fluid Mech.* **685**, 165 (2011).
- <sup>40</sup>M. M. Neamtu-Halic, J.-P. Mollicone, M. Van Reeuwijk, and M. Holzner, "Role of vortical structures for enstrophy and scalar transport in flows with and without stable stratification," *J. Turbul.* **22**, 393 (2021).
- <sup>41</sup>T. Watanabe, R. Jaulino, R. R. Taveira, C. B. da Silva, K. Nagata, and Y. Sakai, "Role of an isolated eddy near the turbulent/non-turbulent interface layer," *Phys. Rev. Fluids* **2**, 094607 (2017).
- <sup>42</sup>K. Nakamura, T. Matsushima, Y. Zheng, K. Nagata, and T. Watanabe, "Large- and small-scale characteristics in a temporally developing shearless turbulent mixing layer," *Phys. Fluids* **34**, 115117 (2022).
- <sup>43</sup>R. D. Moser, M. M. Rogers, and D. W. Ewing, "Self-similarity of time-evolving plane wakes," *J. Fluid Mech.* **367**, 255 (1998).
- <sup>44</sup>P. J. Diamessis, G. R. Spedding, and J. A. Domaradzki, "Similarity scaling and vorticity structure in high-Reynolds-number stably stratified turbulent wakes," *J. Fluid Mech.* **671**, 52 (2011).
- <sup>45</sup>A. Pal and S. Sarkar, "Effect of external turbulence on the evolution of a wake in stratified and unstratified environments," *J. Fluid Mech.* **772**, 361 (2015).
- <sup>46</sup>C. B. da Silva and J. C. F. Pereira, "Invariants of the velocity-gradient, rate-of-strain, and rate-of-rotation tensors across the turbulent/nonturbulent interface in jets," *Phys. Fluids* **20**, 055101 (2008).
- <sup>47</sup>R. Nagata, T. Watanabe, and K. Nagata, "Turbulent/non-turbulent interfaces in temporally evolving compressible planar jets," *Phys. Fluids* **30**, 105109 (2018).
- <sup>48</sup>T. Watanabe, J. J. Riley, K. Nagata, K. Matsuda, and R. Onishi, "Hairpin vortices and highly elongated flow structures in a stably stratified shear layer," *J. Fluid Mech.* **878**, 37 (2019).
- <sup>49</sup>K. Yamamoto, T. Ishida, T. Watanabe, and K. Nagata, "Experimental and numerical investigation of compressibility effects on velocity derivative flatness in turbulence," *Phys. Fluids* **34**, 055101 (2022).
- <sup>50</sup>T. Akao, T. Watanabe, and K. Nagata, "Vertical confinement effects on a fully developed turbulent shear layer," *Phys. Fluids* **34**, 055129 (2022).
- <sup>51</sup>A. Cimarelli, A. Fregni, J.-P. Mollicone, M. van Reeuwijk, and E. De Angelis, "Structure of turbulence in temporal planar jets," *Phys. Fluids* **34**, 045109 (2022).
- <sup>52</sup>T. Watanabe and K. Nagata, "Integral invariants and decay of temporally developing grid turbulence," *Phys. Fluids* **30**, 105111 (2018).
- <sup>53</sup>T. Watanabe, Y. Zheng, and K. Nagata, "The decay of stably stratified grid turbulence in a viscosity-affected stratified flow regime," *J. Fluid Mech.* **946**, A29 (2022).

- <sup>54</sup>G. Comte-Bellot and S. Corrsin, "The use of a contraction to improve the isotropy of grid-generated turbulence," *J. Fluid Mech.* **25**, 657 (1966).
- <sup>55</sup>P.-Å. Krogstad and P. A. Davidson, "Is grid turbulence Saffman turbulence?," *J. Fluid Mech.* **642**, 373 (2010).
- <sup>56</sup>H. Suzuki, K. Nagata, Y. Sakai, and R. Ukai, "High-Schmidt-number scalar transfer in regular and fractal grid turbulence," *Phys. Scr.* **2010**, 014069.
- <sup>57</sup>K. Inokuma, T. Watanabe, K. Nagata, A. Sasoh, and Y. Sakai, "Finite response time of shock wave modulation by turbulence," *Phys. Fluids* **29**, 051701 (2017).
- <sup>58</sup>K. Inokuma, T. Watanabe, K. Nagata, and Y. Sakai, "Statistics of overpressure fluctuations behind a weak shock wave interacting with turbulence," *Phys. Fluids* **31**, 085119 (2019).
- <sup>59</sup>C. S. Shet, M. R. Cholemani, and S. V. Veeravalli, "Optimizing the performance of an active grid to generate high intensity isotropic free stream turbulence," *Phys. Fluids* **32**, 095120 (2020).
- <sup>60</sup>Y. Zheng, K. Nagata, and T. Watanabe, "Energy dissipation and enstrophy production/destruction at very low Reynolds numbers in the final stage of the transition period of decay in grid turbulence," *Phys. Fluids* **33**, 035147 (2021).
- <sup>61</sup>R. E. Britter, J. C. R. Hunt, G. L. Marsh, and W. H. Snyder, "The effects of stable stratification on turbulent diffusion and the decay of grid turbulence," *J. Fluid Mech.* **127**, 27 (1983).
- <sup>62</sup>O. Praud, A. M. Fincham, and J. Sommeria, "Decaying grid turbulence in a strongly stratified fluid," *J. Fluid Mech.* **522**, 1 (2005).
- <sup>63</sup>S. Rahgozar and D. E. Rival, "On turbulence decay of a shear-thinning fluid," *Phys. Fluids* **29**, 123101 (2017).
- <sup>64</sup>A. Kempf, M. Klein, and J. Janicka, "Efficient generation of initial-and inflow-conditions for transient turbulent flows in arbitrary geometries," *Flow, Turbul. Combust.* **74**, 67 (2005).
- <sup>65</sup>T. Kitamura, K. Nagata, Y. Sakai, A. Sasoh, O. Terashima, H. Saito, and T. Harasaki, "On invariants in grid turbulence at moderate Reynolds numbers," *J. Fluid Mech.* **738**, 378 (2014).
- <sup>66</sup>M. Hayashi, T. Watanabe, and K. Nagata, "The relation between shearing motions and the turbulent/non-turbulent interface in a turbulent planar jet," *Phys. Fluids* **33**, 055126 (2021).
- <sup>67</sup>Y. Morinishi, T. S. Lund, O. V. Vasilyev, and P. Moin, "Fully conservative higher order finite difference schemes for incompressible flow," *J. Comput. Phys.* **143**, 90 (1998).
- <sup>68</sup>P. R. Spalart, R. D. Moser, and M. M. Rogers, "Spectral methods for the Navier–Stokes equations with one infinite and two periodic directions," *J. Comput. Phys.* **96**, 297 (1991).
- <sup>69</sup>T. Watanabe, J. J. Riley, K. Nagata, R. Onishi, and K. Matsuda, "A localized turbulent mixing layer in a uniformly stratified environment," *J. Fluid Mech.* **849**, 245 (2018).
- <sup>70</sup>T. Watanabe, X. Zhang, and K. Nagata, "Direct numerical simulation of incompressible turbulent boundary layers and planar jets at high Reynolds numbers initialized with implicit large eddy simulation," *Comput. Fluids* **194**, 104314 (2019).
- <sup>71</sup>K. Nagata, H. Suzuki, Y. Sakai, T. Hayase, and T. Kubo, "Direct numerical simulation of turbulent mixing in grid-generated turbulence," *Phys. Scr.* **T132**, 014054 (2008).
- <sup>72</sup>S. Laizet and J. C. Vassilicos, "DNS of fractal-generated turbulence," *Flow, Turbul. Combust.* **87**, 673 (2011).
- <sup>73</sup>H. Suzuki, K. Nagata, Y. Sakai, T. Hayase, Y. Hasegawa, and T. Ushijima, "Direct numerical simulation of fractal-generated turbulence," *Fluid Dyn. Res.* **45**, 061409 (2013).
- <sup>74</sup>L. Djenidi, S. F. Tardu, and R. A. Antonia, "Relationship between temporal and spatial averages in grid turbulence," *J. Fluid Mech.* **730**, 593 (2013).
- <sup>75</sup>T. Watanabe, Y. Sakai, K. Nagata, Y. Ito, and T. Hayase, "Implicit large eddy simulation of a scalar mixing layer in fractal grid turbulence," *Phys. Scr.* **91**, 074007 (2016).
- <sup>76</sup>M. Wang, T. Yurikusa, Y. Sakai, K. Iwano, Y. Ito, Y. Zhou, and Y. Hattori, "Interscale transfer of turbulent energy in grid-generated turbulence with low Reynolds numbers," *Int. J. Heat Fluid Flow* **97**, 109031 (2022).
- <sup>77</sup>M. Anas, P. Joshi, and M. K. Verma, "Freely decaying turbulence in a finite domain at finite Reynolds number," *Phys. Fluids* **32**, 095109 (2020).
- <sup>78</sup>T. Watanabe and K. Nagata, "Energetics and vortex structures near small-scale shear layers in turbulence," *Phys. Fluids* **34**, 095114 (2022).
- <sup>79</sup>M. Gampert, J. Boschung, F. Hennig, M. Gauding, and N. Peters, "The vorticity versus the scalar criterion for the detection of the turbulent/non-turbulent interface," *J. Fluid Mech.* **750**, 578 (2014).
- <sup>80</sup>T. Watanabe, Y. Sakai, K. Nagata, Y. Ito, and T. Hayase, "Turbulent mixing of passive scalar near turbulent and non-turbulent interface in mixing layers," *Phys. Fluids* **27**, 085109 (2015).
- <sup>81</sup>M. Gampert, V. Narayanaswamy, P. Schaefer, and N. Peters, "Conditional statistics of the turbulent/non-turbulent interface in a jet flow," *J. Fluid Mech.* **731**, 615 (2013).
- <sup>82</sup>M. Hayashi, T. Watanabe, and K. Nagata, "Characteristics of small-scale shear layers in a temporally evolving turbulent planar jet," *J. Fluid Mech.* **920**, A38 (2021).
- <sup>83</sup>K. Horiuti and Y. Takagi, "Identification method for vortex sheet structures in turbulent flows," *Phys. Fluids* **17**, 121703 (2005).
- <sup>84</sup>O. R. H. Buxton and B. Ganapathisubramani, "Amplification of enstrophy in the far field of an axisymmetric turbulent jet," *J. Fluid Mech.* **651**, 483 (2010).
- <sup>85</sup>S. Pirozzoli, M. Bernardini, and F. Grasso, "On the dynamical relevance of coherent vortical structures in turbulent boundary layers," *J. Fluid Mech.* **648**, 325 (2010).
- <sup>86</sup>K. Bhatt and Y. Tsuji, "Identification of vortex structures in flow fields using tomographic PIV method," *J. Fluid Sci. Technol.* **16**, JFST0018 (2021).
- <sup>87</sup>T. Watanabe, K. Tanaka, and K. Nagata, "Characteristics of shearing motions in incompressible isotropic turbulence," *Phys. Rev. Fluids* **5**, 072601 (2020).
- <sup>88</sup>D. Fiscaletti, O. R. H. Buxton, and A. Attili, "Internal layers in turbulent free-shear flows," *Phys. Rev. Fluids* **6**, 034612 (2021).
- <sup>89</sup>S.-J. Kang, M. Tanahashi, and T. Miyauchi, "Dynamics of fine scale eddy clusters in turbulent channel flows," *J. Turbul.* **8**, N52 (2007).
- <sup>90</sup>A. A. Ghira, G. E. Elsinga, and C. B. da Silva, "Characteristics of the intense vorticity structures in isotropic turbulence at high Reynolds numbers," *Phys. Rev. Fluids* **7**, 104605 (2022).
- <sup>91</sup>C. Dopazo, J. Martín, and J. Hierro, "Local geometry of isoscalar surfaces," *Phys. Rev. E* **76**, 056316 (2007).
- <sup>92</sup>C. Meneveau and K. R. Sreenivasan, "Interface dimension in intermittent turbulence," *Phys. Rev. A* **41**, 2246 (1990).
- <sup>93</sup>B. C. Blakeley, B. J. Olson, and J. J. Riley, "Self-similarity of scalar isosurface area density in a temporal mixing layer," *J. Fluid Mech.* **951**, A44 (2022).
- <sup>94</sup>B. C. Blakeley, W. Wang, and J. J. Riley, "On the kinematics of scalar iso-surfaces in decaying homogeneous, isotropic turbulence," *J. Turbul.* **20**, 661 (2019).
- <sup>95</sup>R. Sahebjam, K. F. Kohan, and S. Gaskin, "The dynamics of an axisymmetric turbulent jet in ambient turbulence interpreted from the passive scalar field statistics," *Phys. Fluids* **34**, 015129 (2022).
- <sup>96</sup>J. Philip and I. Marusic, "Large-scale eddies and their role in entrainment in turbulent jets and wakes," *Phys. Fluids* **24**, 055108 (2012).